



**CHALMERS**  
UNIVERSITY OF TECHNOLOGY

## **Microstructure and Properties of FeCrAl Overlay Welds at High Temperature Service**

Downloaded from: <https://research.chalmers.se>, 2025-07-01 04:17 UTC

Citation for the original published paper (version of record):

Valiente Bermejo, M., Thuvander, M. (2025). Microstructure and Properties of FeCrAl Overlay Welds at High Temperature Service. Metallurgical and Materials Transactions A: Physical Metallurgy and Materials Science, In Press. <http://dx.doi.org/10.1007/s11661-025-07846-w>

N.B. When citing this work, cite the original published paper.

# Microstructure and Properties of FeCrAl Overlay Welds at High Temperature Service



M.A. VALIENTE BERMEJO and M. THUVANDER

Recently developed FeCrAl alloys could be an economical alternative to nickel-based alloys in overlay welds for the power generation industry. However, more investigation on their microstructure and properties is needed at temperatures for boiler applications. This work compared the performance of three FeCrAl alloys (EF100, EF101, and APMT) as overlay welds, in as-deposited condition and after being exposed for 6 months in a CFB boiler's evaporator tube bank. Bending, high temperature tensile test, restraint-cooling test, hardness, fractography, microscopy, microanalysis, and atom probe tomography (APT) were used. The results showed a ranking for ductility, being EF100 > EF101 > APMT. A high ductile-to-brittle transition temperature, below 100 °C, confirmed the low ductility and high cold cracking susceptibility. The microstructural analysis was in line with the previous grading. For APMT, APT showed that the exposure of the alloy at 400 °C for 11 days resulted in higher Cr concentration around carbides than in the matrix. This suggests that carbides could be initiation sites pushing toward the  $\alpha$ -phase separation (Fe-rich vs Cr-rich), explaining the hardening and resulting in a drastic reduction in the ductility of APMT overlay welds.

<https://doi.org/10.1007/s11661-025-07846-w>  
© The Author(s) 2025

## I. INTRODUCTION

RESEARCH on high temperature materials is of great interest not only to the energy production sector, but also to fund providers and stakeholders who are seeking to increase the economic and ecological sustainability of energy production.<sup>[1–4]</sup>

FeCrAl alloys are ferritic iron–chromium–aluminum alloys developed for use at temperatures up to around 1400 °C in air.<sup>[5,6]</sup> Their chromium and aluminum content promotes the formation of protective oxide scales at temperatures above 900 °C.<sup>[7–9]</sup> Therefore, their potential fields of application are found in the power generation industry for the fabrication of boilers, furnaces, radiant tubes, furnace fittings, but also in heaters at heat treatment industries, in high temperature process plants, concentrated solar power plants, and the nuclear industry.

In the field of nuclear power generation, FeCrAl alloys have been considered for reactor core internal applications and as claddings because of their oxidation and corrosion resistance at high temperature, their radiation-induced cavity swelling resistance, high resistance to stress corrosion cracking and maintenance of mechanical properties at and above typical light water reactor temperatures.<sup>[10–15]</sup> Their slow oxidation kinetics at high temperatures allows the eventual FeCrAl cladding to remain intact longer, making accident mitigation more likely.

In the field of waste incineration plants, low-alloyed carbon steels are normally used as structural material in the furnace walls and in the banks of tubes that form the superheaters and evaporators. However, the combustion of biomass produces an environment with high concentrations of alkali metals, chlorine, and heavy metals that corrode low-alloyed steels.<sup>[16,17]</sup> Cladding the low-alloyed carbon steels with corrosion-resistant alloys, such as the nickel-based alloy EN Ni6625, known as alloy 625, is the commonly used alternative. FeCrAl alloys would be a more economical alternative to nickel-based alloys if they could withstand the harsh waste incineration environment. In line with this, some research works<sup>[17,18]</sup> evaluated the corrosion resistance of several alloys under different furnace conditions. The results showed that tubes of FeCrAl alloy Kanthal® APMT (Fe21 Cr5 Al3Mo) had a lower corrosion rate than alloys such as AISI 310S and EN 10028 16Mo3, and also slightly lower than nickel-based alloy EN Ni6625.

---

M.A. VALIENTE BERMEJO is with the Department of Engineering Science, University West, Gustava Melins Gata 2, 461 32, Trollhättan, Sweden. Contact e-mail: [asun.valiente@hv.se](mailto:asun.valiente@hv.se). M. THUVANDER is with the Department of Physics, Chalmers University of Technology, 412 96, Gothenburg, Sweden. Contact e-mail: [mattias.thuvander@chalmers.se](mailto:mattias.thuvander@chalmers.se). Manuscript submitted December 17, 2024; accepted May 16, 2025.

These promising results positioned the FeCrAl alloys as candidates to be used in tube claddings in waste incineration plants.

Two main challenges concerning FeCrAl alloys still need further investigation. On one hand, the weldability of new FeCrAl alloys is still to be optimized. Regina and Dupont<sup>[19,20]</sup> studied the susceptibility to hydrogen cracking of FeCrAl overlay claddings. Not only can the formation of the inherently brittle intermetallic compounds of Fe<sub>3</sub>Al and FeAl can induce cracking, but the welding process and type of consumable selected can also influence the hydrogen content in the weld. The presence of (Fe, Cr) x C and (Fe, Al)<sub>3</sub> C type carbides was found to improve the cracking resistance to the point where crack-free welds could be obtained on some overlays that contained the brittle intermetallic phases. Another challenge is the eventual phase separation and consequent embrittlement that FeCrAl alloys can experience in the range of exposure temperatures in waste incineration plants applications. The influence of aluminum on the suppression of the 475 °C embrittlement of FeCrAl alloys<sup>[21,22]</sup> and specifically the kinetics of Fe-rich ( $\alpha$ ) and Cr-rich ( $\alpha'$ ) phase separation in these alloys has been studied.<sup>[23–25]</sup>

There are different novel aspects in this research. On one hand, it is not FeCrAl tubes in as-delivered condition that are investigated but overlay welds of FeCrAl alloys on a carbon steel substrate. The rapid solidification conditions and the response of the FeCrAl alloys to the stresses associated with welding will determine the resulting microstructure and properties of those overlays. This knowledge gap needs to be filled to determine if FeCrAl alloys can be an alternative to the current Ni-based alloys used in boiler applications. On the other hand, out of the three FeCrAl alloys investigated, two were newly developed and were not in the market when the work was conducted, therefore, publications on the new alloys are limited. Another novel aspect in this work is the fact that overlay welds were exposed on-site on evaporator tubes of a boiler for 6 months, instead of using conventional small-scale laboratory tests to simulate the exposure conditions. This research aims to bring new knowledge on the properties of FeCrAl overlay welds in the range of boiler application temperatures.

## II. EXPERIMENTAL

In this chapter, the materials, the welding process to produce the overlay welds, and the exposure in the boiler are described. The microstructure and hardness of the overlay welds were investigated before and after being exposed on-site on evaporator tubes of a boiler. However, to obtain information on additional properties of the overlay welded material, further in-lab tests were conducted. The ductility was assessed using bend testing and fractographic inspection of the resulting surfaces. To complement the information about ductility, a thermo-mechanical simulator was used to evaluate

the tensile properties at different temperatures. During welding, the expansion caused by the heating and the contraction caused by the cooling, originate residual stresses in the welds. The effect of those stresses has not been monitored earlier for FeCrAl alloys, and for that purpose, a restraint-cooling test was designed and conducted. Finally, some as-deposited welds were heat treated in a furnace to investigate the eventual hardening and softening mechanisms using Atom Probe Tomography (APT).

### A. Materials

The substrate and the different cladding materials used were as follows:

The substrate was the low-alloyed Cr–Mo steel grade 16Mo3 (EN 10028-2) in the form of 4 mm thickness, 48.3 mm outer diameter, and 2-meter length tubes for the preparation of the tube shields and in the form of 4 mm thickness plates for the preparation of samples for the in-lab tests (*i.e.*, bend test, high temperature tensile test, and the restraint-cooling test). This is a structural carbon steel with molybdenum content between 0.25 and 0.35 wt pct for service temperatures below 500 °C.

Three Kanthal® FeCrAl alloys designated as EF101, EF100, and APMT in the form of 1.2 mm  $\phi$  solid wires were used as cladding materials. Table I shows the nominal chemical composition of these FeCrAl wires. The FeCrAl alloys also contain additions of reactive elements (RE) intended to improve oxidation resistance, which cannot be disclosed due to intellectual property rights. Sanicro® 625 (AWS/SFA-5.14 ERNiCrMo-3, EN ISO 18274 G Ni 6625), commonly known as alloy 625 in the form of 1.2 mm  $\phi$  solid wire, was used as reference material for comparison.

### B. Welding

Mechanized Gas Metal Arc Welding (GMAW) was used to prepare overlay welds on the 16Mo3 substrate. In all cases, the overlay welds were prepared to cover the entire substrate surface. The power source was a TPS 5000 CMT coupled with a robotic arm, and the shielding gas was pure argon (99.99 pct) at a gas flow of 15 l/min.

For the FeCrAl alloys, one-layer claddings were prepared (Figure 1). The average thickness of the one-layer clads was 3 mm. For alloy 625, a two-layer cladding was needed for Alloy 625, to avoid exceeding the maximum limit of 5 to 10 pct iron content in the overlay due to the dilution with the 16Mo3 substrate. A higher iron content in this nickel-based alloy would be detrimental to its corrosion resistance.<sup>[26,27]</sup> The average thickness of the two-layer cladding was 6 mm.

The welds were performed at DCEP polarity, and the welding settings were as follows: current 160 to 200 A, 22 V, wire feed speed 6.3 to 7.2 m/min, welding speed 480 mm/min, stick out 12 to 14 mm, and the interpass temperature was kept below 150 °C.

**Table I. Chemical Composition of the Wires (Wt Pct)**

Alloy	Cr	Al	Si	Mn	C	Mo	Fe	Ni	Nb
Kanthal® EF100	10.0	4.0	0.3	< 0.7	< 0.08		bal.		
Kanthal® EF101	12.5	3.7	1.3	< 0.7	< 0.08		bal.		
Kanthal® APMT	21.0	5.0	< 0.7	< 0.4	< 0.08	3.0	bal.		
Alloy 625	22.1	0.1	0.1	0.1	0.01	9.1	0.4	64.2	3.5

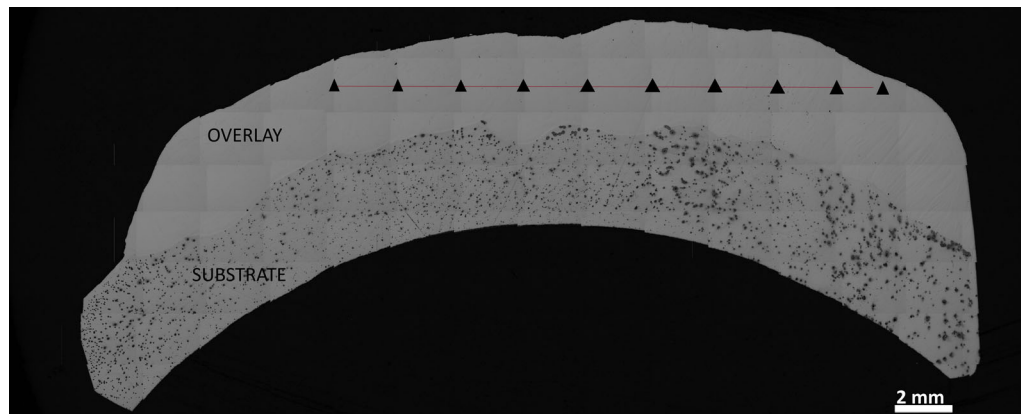


Fig. 1—Cross-section of the tube shield, showing the substrate and the overlay weld. Ten indent locations in a horizontal pattern along the overlay center line. Outer locations are positioned closer to the surface, and inner locations come toward the inner part of the overlay, being the central location closer to the fusion boundary with the substrate.

**Table II. Operational Conditions**

HCl in Flue Gas (mg/ Nm <sup>3</sup> )	SO <sub>2</sub> in Flue Gas (mg/ Nm <sup>3</sup> )	H <sub>2</sub> O in Flue Gas (vol Pct)	O <sub>2</sub> in Flue Gas Left Side (vol Pct)	O <sub>2</sub> in Flue Gas Right Side (vol Pct)
507 ± 145	16 ± 41	15 ± 3	6 ± 1	6 ± 1

### C. On-Site Exposures

The exposure of the overlay welded tube shields took place in the evaporator tube bank of the waste-fired combined heat and power plant designated as P14 at Händelö, E.ON utility, Norrköping, Sweden. The boiler is a 75 MW circulating fluidized bed (CFB) boiler generating steam with 65 bar pressure and a final temperature of 450 °C. It uses a fuel mix of 30 to 50 pct combined household waste and 50 to 70 pct of classified industrial waste.

During the 6-month exposure period, the sensors in the boiler continuously monitored several operational parameters such as the steam temperature, and the concentration of HCl, SO<sub>2</sub>, humidity, and oxygen in the flue gas. A complete set of data was extracted every 30 minutes to analyze the exposure conditions in this work. The average values for the operational data during the 6-month exposure are shown in Table II. These values only refer to the steady-state regime. The flue gas temperature varied within the interval 510 °C to 690 °C, and it was measured to be on average 620 °C at the location of the exposed tube shields.

Inside the evaporator tubes, where the tube shields were mounted, the temperature of the water corresponds to the saturation temperature at the operational pressure of the boiler, which was 281 °C. The temperature of the tubes is estimated to be 30 °C to 50 °C above this temperature, and the temperature of the tube shields is estimated to be somewhat above that temperature, with some variations caused by possible differences in contact between the tube shields and the tubes.

### D. Testing of On-Site Exposed Samples: Hardness and Microstructure

Hardness testing and microstructure inspection were conducted on the overlay welds before and after being exposed in the boiler for 6 months.

The hardness tester was a Struers Duramin 40 AC1 previously calibrated (calibration block 304±6.5 HV<sub>0.5</sub>). Vickers hardness was chosen with an applied load of 300 g and 10 seconds dwell time. Ten individual measurements were conducted along the center line of the layer (Figure 1). As the clads were deposited on a tube, that pattern gave the possibility to have measurements in

positions closer to the surface and positions closer to the fusion boundary, with maybe local differences in the chemical composition (due to dilution or to diffusion of certain elements during the exposure). Therefore, that testing pattern is expected to give a representative overall hardness value for the overlay.

Hardness testing was also conducted following the same equipment and procedure (10 indents) on the samples selected for aging heat treatment (see the “[Aging Heat Treatments and Atom Probe Tomography \(APT\)](#)” section).

In terms of microstructural inspection, light optical microscopy (LOM) Zeiss Axio Imager.M2 m, and Olympus BX60M were used in this work. For FeCrAl overlay welds, two etchants were found suitable: Aqua Regia (100 mL HNO<sub>3</sub> 60 pct + 100 mL HCl 37 pct) immersed for 3 to 5 seconds and Kalling’s n<sup>o</sup>2 (5 g CuCl<sub>2</sub> + 100 mL HCl + 100 mL ethanol) for 4 seconds (APMT) and 8 seconds (EF100 and EF101).

Zeiss EVO 50 and FE-SEM Gemini 450 were the two Scanning Electron Microscopes (SEM) equipped with energy dispersive X-ray (EDS) used in this work.

### E. In Lab Testing

The purpose of conducting the lab tests below was to evaluate different properties of undiluted FeCrAl clad material, without interferences from the substrate. The influence of temperature on the tensile properties, the ductility, and the response of the material to different cooling rates and restraint conditions was investigated. Undiluted clad material was exposed to aging and examined by APT to propose a mechanism behind the hardening evolution of the alloys under boiler conditions. For all these experiments, overlay welded specimens were prepared on 16Mo3 sheets of the same thickness as the tube shields in the boiler, 4 mm, and by using the same welding parameters and shielding gas as described in the “[Welding](#)” section. The reasons to prepare overlay welds on flat specimens were to conduct the tests in accordance with specific standards, ensuring the easy extraction of undiluted as-deposited FeCrAl weld metal from the substrate.

#### 1. Face-bend testing and fractography

The surface of the clad coupons was machined to ensure a flat surface suitable for face-bend testing. The maximum bending angle to fracture was measured as an indication of the ductility of the different overlay welds.

The test was conducted according to ISO 5173:2010 at room temperature using a Zwick/Roell Z100 equipment. The specimens’ size was 230 mm length, 43 mm width, and 6 mm thickness (4 mm thickness of 16Mo3 substrate + 2 mm thickness of the investigated alloy after machining). The specimens were placed on two parallel support rollers of 50 mm diameter. They were centered in length and width, and with the 16Mo3 substrate side facing the die so that the clad material was in tension during the test. The die used was 30 mm in diameter, therefore, the distance between the rollers was fixed to 48 mm following ISO 5173.

The fracture surface of the bend test samples was investigated using a SEM Zeiss EVO 50.

#### 2. Restraint-cooling test

The purpose was to investigate the response of FeCrAl undiluted welds to restraint and cooling conditions simulating those taking place in fusion processes such as overlay welding. If restraint and cooling rates could be correlated with resulting cracking susceptibility, it should be possible to act on the welding settings to minimize the cracking in the deposited material. The initial intention was to simulate cooling rates in the order of the laser processing (1,000 °C/s to 10,000 °C/s). However, that was not feasible with the configuration available in our thermo-mechanical simulator (Gleeble, Dynamic Systems, Inc.). Instead, 100 °C/s and 10 °C/s were the cooling rates selected as they were in the order of magnitude for arc welding and casting, respectively.

Two-layer clads were prepared on the substrate plates (4 mm thickness 16Mo3) (see Figure 2). Afterward, the substrate and 3 mm of the first layer were machined off. The remaining undiluted clad material, which was 3 mm thick, was cut in the transverse direction (perpendicular to the deposition direction) and machined according to Figure 3.

The coupons were rapidly heated to 1200 °C (in 3.6 seconds), then cooled at two different rates: 100 °C/s and 10 °C/s. To monitor the temperature, one thermocouple was attached in the center of the parallel length (Figure 3).

For each of the two cooling rates, two restraint conditions were applied:

- In the “maximum restraint,” the coupon was tightly gripped, without the possibility of expanding or contracting. In this experiment, the force in the grips was recorded *vs* the temperature.
- In the “no restraint,” the coupon was free to deform. In this experiment, the position, and therefore the deformation, was recorded *vs* the temperature.

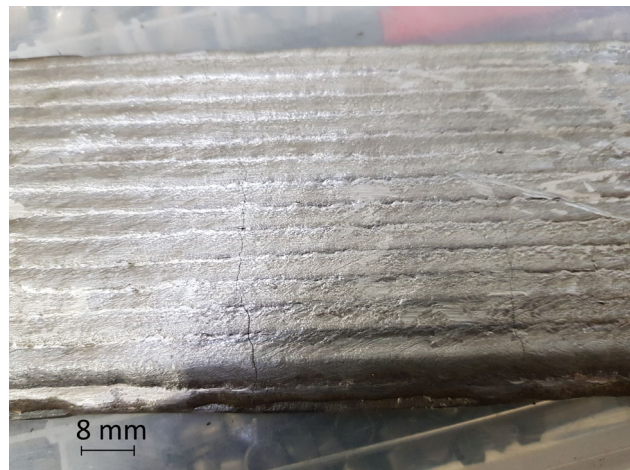


Fig. 2—2-layer overlay clad produced with EF101 before machining.

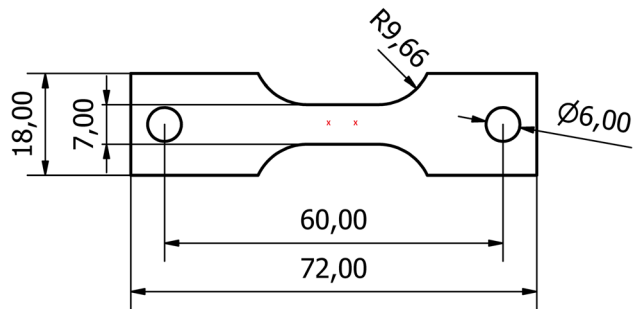


Fig. 3—Sketch of the coupons used in the restraint-cooling test (dimensions in mm). The red crosses show the location of the thermocouples attached at the center of the parallel length.

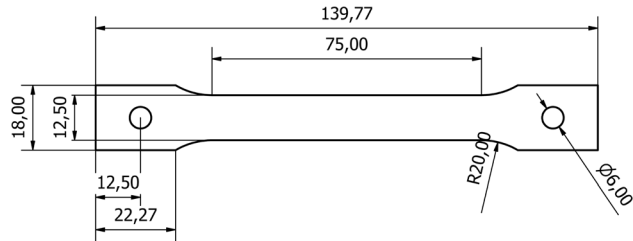


Fig. 4—Sketch of the coupons used in the high temperature tensile test (dimensions in mm).

**Table III. Tensile Testing Conditions and Number of Specimens**

Overlay Material	Temperature (°C)	Number of Coupons
APMT	RT	2
	100	2
	200	2
	400	2
EF100	RT	3
	100	3
	200	3
	400	3

### 3. High temperature tensile test

The influence of the temperature on the strength and ductility of undiluted FeCrAl material is important when assessing the feasibility of using these alloys in boiler applications.

To test undiluted deposited material, the samples were produced using the same procedure outlined in the “[Restraint-cooling Test](#)” section. The only difference was the coupons’ size (Figure 4). The high temperature tensile test required a longer parallel length to enable the attachment of three thermocouples to confirm the homogeneity of the temperature in the parallel length and to attach the extensometer. ISO 6892-1 standard (method B, strain rate 0.0012/s, stress rate approx. 20 MPa/s) was followed in a thermo-mechanical simulator (Gleeble, Dynamic Systems Inc.). In the last stages of cutting and machining, all the EF101 overlay welds cracked; therefore, it was not possible to conduct the tensile tests on EF101 material. Similarly, some APMT samples cracked during the cutting and machining stage,

**Table IV. Heat Treatment Conditions**

Overlay Material	Temperature (°C)	Time (Days)	Cooling
APMT	400	11	Air
EF100	400	11	Air
		42	Air

and it was not possible to have 3 repetitions for each testing condition.

The samples were rapidly heated to the target temperatures (400 °C, 200 °C, 100 °C). After the tensile test, the samples were air-quenched at 100 °C/s. Tensile tests were also conducted at room temperature (RT). Table III shows the testing conditions and number of specimens tested.

### 4. Aging heat treatments and Atom Probe Tomography (APT)

To investigate the reasons behind the hardening in APMT and the softening in EF100 overlays caused by the exposure in the boiler, it was decided to conduct heat treatments in the laboratory, followed by Atom Probe Tomography (APT) inspection.

The samples used for the heat treatment were undiluted deposited material produced as described in the “[Restraint-cooling Test](#)” section. The temperature was set to 400 °C, based on the estimated temperature experienced by the tube shields in the boiler, and considering that 475 °C embrittlement and phase separation phenomena should be evaluated.

The heat treatments were conducted in a Vecstar Ltd. furnace model LF2, and Table IV lists the heat treatment conditions.

The undiluted deposited FeCrAl specimens APMT and EF100 in both the as-welded and heat-treated conditions were investigated with APT. For APT preparation, small plates were ground to a thickness of 0.3 mm and a size of 15 × 0.3 × 0.3 mm<sup>3</sup> by using a low-speed saw. Afterward, needle-shaped specimens were prepared by a two-stage electropolishing procedure. The analyses were performed using a LEAP 6000 XR (Cameca), in laser pulse mode. The laser power was 30 pJ, the temperature was 50 K, and the detection rate was 0.5 pct. The software AP Suit 6.3 was used for making reconstructions and to analyzing the data.

## III. RESULTS

In this chapter, the results are presented in three blocks. The first block focuses on the evaluation of the ductility of the overlay welds, and it comprises the results of the bend test, fractography, and the high temperature tensile test. The second block is also related to ductility, but it focuses on simulating the influence of the cooling rate and the restraint conditions during the overlay welding process. Finally, the third block presents the evolution of hardness and microstructure caused by the exposure in the boiler, and the complementary investigation of the eventual hardness changes with the laboratory heat treatment, followed by APT.

### A. Ductility of the Overlay Welds: Bend Test, Fractography, and High Temperature Tensile Test

The bend test results reveal that alloy 625 has the highest ductility, as it was fully bent to 135 deg without fracture. Among the FeCrAl overlays, EF100 showed the highest ductility, bending up to 75 deg before fracture, and APMT presented the lowest ductility with only 4 deg bending before fracture. The bending angle to fracture and the maximum force applied are shown in Table V. As an illustration, Figure 5 shows an image of the specimens after the bend test.

The fracture surfaces of the three FeCrAl overlay welds show the same pattern (Figure 6): cleavage fracture mode in the overlay section and a transition to dimple rupture in the boundary with the 16Mo3 substrate. Higher magnification images of the fusion boundary are shown in Figure 7. In the FeCrAl sections, the fracture path is mainly transgranular [Figure 8(a)] following the Z axis (vertical). It is also possible to observe transverse cracks in the X axis (horizontal) to the main crack plane (Z axis), as illustrated in Figure 8(b). This crack path is likely the most energetically efficient way to orient the macroscopic crack plane perpendicular to the largest principal stress while isolating the cracking along the same weak crystallographic plane on the local scale. A similar observation was made by Chao and Capdevila.<sup>[28]</sup>

As a difference with EF100 and EF101, the fracture surface of the APMT overlay welds shows additional cracks in the Y axis, perpendicular to both the Z (vertical) and the X (horizontal). Those cracks propagate inwards (Figure 9).

Concerning the tensile testing of the undiluted clad material, only APMT and EF100 were tested, as it was not possible to obtain EF101 coupons with the parallel length free from cracks.

Just by a visual inspection of the coupons after the tensile testing, the difference in ductility was evident. The APMT specimens showed very little or no plastic deformation, while in EF100, there was plastic deformation (necking, cup and cone) (Figure 10), indicating a more ductile fracture than in APMT.

The difference in ductility is also evident when comparing the stress-strain diagrams (Figure 11). In EF100, it is possible to see the effect of the necking after the ultimate tensile strength, while the APMT diagram does not show plastic deformation. Table VI compiles the yield strength, ultimate tensile strength, and elongation obtained from the diagrams.

In both materials, APMT and EF100, an increase in the test temperature leads to a reduction in the yield strength. There is an important difference in APMT when tested at 400 °C, as the material becomes even more brittle and does not show any sign of elastic behavior.

The results (Table VI and Figure 11) suggest that both materials have a high ductile-to-brittle transition temperature, somewhere between room temperature and 100 °C, which is an indication of low ductility and therefore high cold cracking susceptibility of these alloys.

The first block of results, considering the bending angle to fracture, the fracture morphology, and the tensile tests, indicate that the FeCrAl overlay welds could be graded from higher to lower ductility as follows: EF100 > EF101 > APMT.

### B. Influence of Cooling Rate and Restraint Conditions on the Ductility of FeCrAl Undiluted Overlays

As described in the “[Restraint-cooling Test](#)” section, the thermo-mechanical simulator heated the undiluted FeCrAl samples to 1200 °C very fast (in 3.6 seconds), and then two different cooling rates were imposed (100 °C/s and 10 °C/s) in combination with two restraint conditions (maximum restraint applied in the jaws and with no restraint to the movement of the jaws).

The behavior and response of the material (stress in the max restraint conditions or deformation in the no restraint conditions) vs the temperature showed the same pattern, regardless of the type of FeCrAl overlay. As an example, Figure 12 shows the evolution of deformation and stress vs temperature for APMT, and Figure 13 shows the comparison of the results for the different alloys. In the no-restraint conditions [Figures 12(c) and (d)], the FeCrAl alloys expanded during the heating and reached their maximum expansion at the maximum temperature. After a few seconds, the material started to experience contraction during the cooling. The slope or speed of contraction for each material was found to be dependent on the alloy [Figure 13(d)], because thermal expansion is an intrinsic property for each alloy at each temperature, but also dependent on the cooling rate used, being the higher the cooling rate, the faster the contraction of the material. The larger difference in the contraction rate took place at the higher cooling rate (100 °C/s). The alloy that showed a faster slope or speed of contraction was APMT, followed by EF101, and the one with the slowest slope of contraction was EF100. EF100 was the alloy that deformed less at 10 °C/s [Figure 13(c)].

In the maximum restraint experiments, which are closer to conditions of restraints experienced in welding [Figures 12(a) and (b)], the jaws gave opposition to the expansion of the material during the heating, and compressive stresses were registered in the jaws. Afterward, during the subsequent cooling, an increase in the tensile stresses was registered. The final level of residual stress was found to be very similar (around 180 MPa) for all the FeCrAl alloys at the slower cooling rate (10 °C/s), but at the higher cooling rate (100 °C/s) EF100 overlay was able to withstand higher stresses (close to 50 MPa) than the rest of the FeCrAl overlays.

This second block of results indicated that EF100 overlay material can withstand higher stresses than the rest of the FeCrAl alloys under high restraint conditions and fast cooling rates simulating welding conditions. Under no restraint conditions, this is also the alloy that shows the slowest rate of deformation/contraction during cooling. The response of APMT and EF101 overlays revealed less capability to cope with stresses under cooling, and they showed faster rates of contraction. The results also show that in conditions of slow

**Table V. Bending Angle to Fracture and Maximum Force Applied to Fracture**

Specimen	Bending Angle (Deg)	Max Force (kN)
EF100	75	13
EF101	16	12
APMT	4	8.5
Alloy 625	full bend (135 deg) without cracking	21

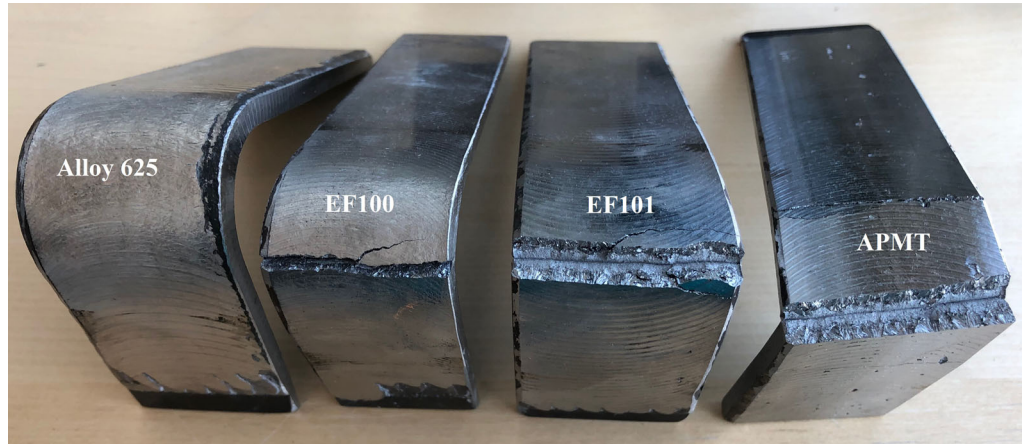


Fig. 5—Image of the specimens after the bend test. From left to right: specimens clad with Alloy 625, EF100, EF101, and APMT, in order from the highest to the lowest ductility.

cooling, which are more similar to casting, the three FeCrAl overlays could withstand a similar level of stresses.

### C. Influence of Temperature on Microstructure and Hardness

This block of results includes the evolution of hardness and microstructure caused by the exposure of the overlay welds in the boiler, and the complementary investigation of the eventual hardness changes with the laboratory heat treatment, followed by APT investigation.

The hardness was measured in the overlay weld produced with alloy 625 and in the overlay welds produced with the three FeCrAl alloys. By comparing the hardness values in the as-deposited (non-exposed) and the exposed condition (in the tube shield for 6 months), it should be possible to get indications of an eventual change in the microstructure of the overlay welds based on the time and temperature conditions of the exposure. Figure 14 shows the individual hardness results obtained according to the experimental procedure (see the “[Testing of On-site Exposed Samples: Hardness and Microstructure](#)” section, Figure 1) and the hardness resulting from the furnace exposure. The vertical scale in Figure 14 was kept constant for a clearer visualization of the hardness differences among the alloys.

From these results, the overlay welds can be ordered from higher to lower hardness as follows: APMT > alloy 625 > EF101 > EF100. It is noticeable that the highest hardness corresponds to APMT in exposed condition ( $330 \pm 27 \text{ HV}_{0.3}$ ), followed by alloy 625.

To determine if the change in hardness due to the boiler exposure was significant or not in these alloys, the mean values and the relative variation of the mean values were calculated  $\left[ \frac{(\text{mean value after exposure}) - (\text{mean value before exposure})}{(\text{mean value before exposure})} \times 100 \right]$ . The coefficient of variation pct (standard deviation/mean value  $\times 100$ ) is calculated as a measure of data spread and confidence in the relative variation of the mean values. For APMT overlay welds, when comparing the hardness variation between the as-deposited and the exposed condition, the mean value experienced an increase of 22 pct (from 269 to 330  $\text{HV}_{0.3}$ ), and the coefficient of dispersion ranged from 4 pct in the as-deposited to 8 pct after exposure. The trend was the opposite in the overlay welds of EF100, as the mean value showed a decrease of 17 pct (from 234 to 193  $\text{HV}_{0.3}$ ), and the coefficient of dispersion was 5 pct for both as-deposited and after exposure. Results confirm that the exposure in the boiler resulted in hardening of the APMT overlay and softening of the EF100 overlay.

In case of overlay welds of EF101 and alloy 625, there seems to be a minor increase in the hardness mean values (5.4 and 2.6 pct, respectively) after the exposure in the boiler. The coefficient of variation was 5 pct for EF101 in as-deposited and after exposure, and from 3 to 5 pct for alloy 625 in as-deposited and after exposure, respectively. The small increase in the variation of the mean values, together with the low spread in the results, indicates that it is not possible to confirm that the exposure has had a clear influence on the resulting hardness.

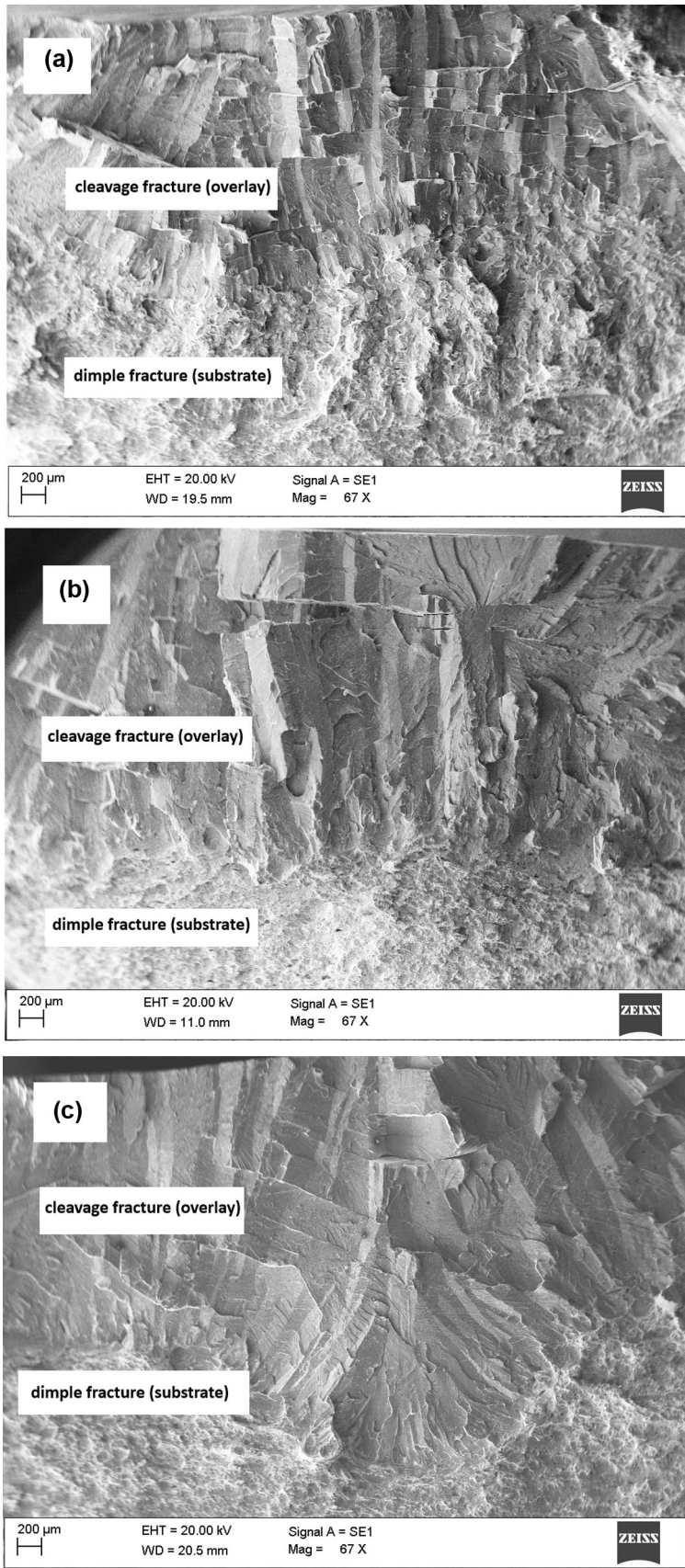


Fig. 6—Fracture morphology of the overlay welds at the same magnification (X67). (a) corresponds to EF100, (b) corresponds to EF101, and (c) corresponds to APMT.

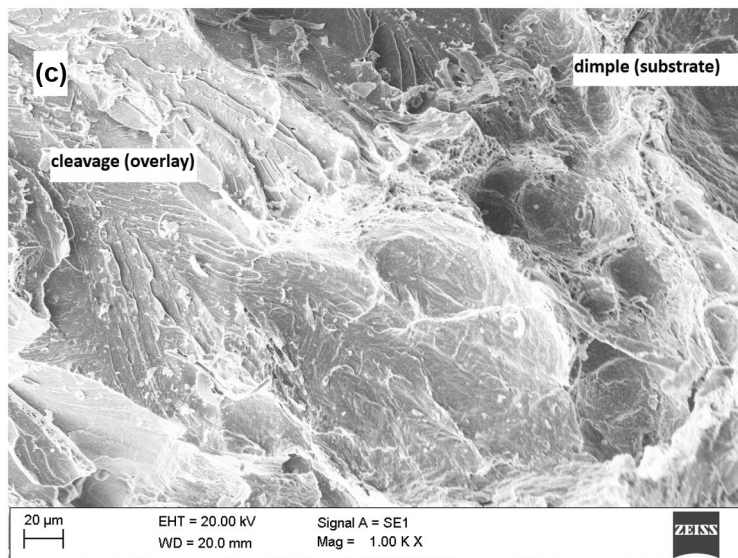
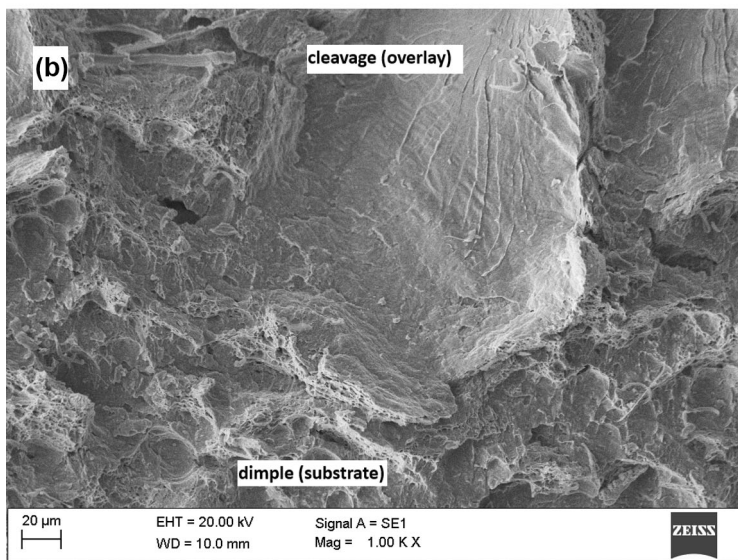
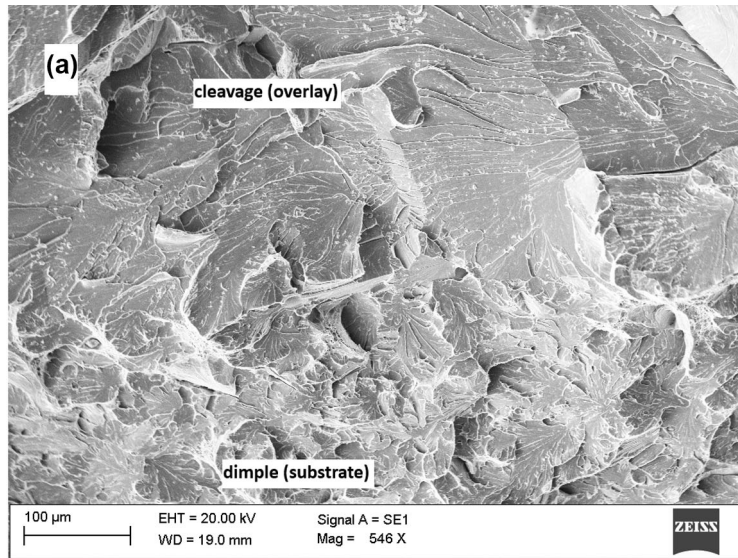


Fig. 7—Higher magnification of the fusion boundary, showing the transition from brittle cleavage in the overlay weld, to more ductile dimple fracture in the substrate. (a) corresponds to EF100, (b) corresponds to EF101, and (c) corresponds to APMT.

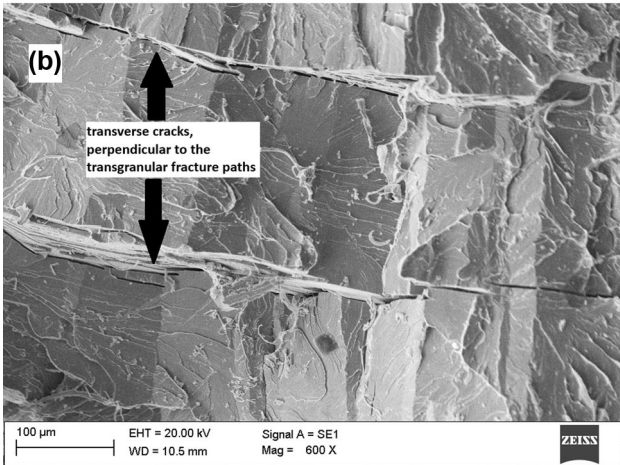
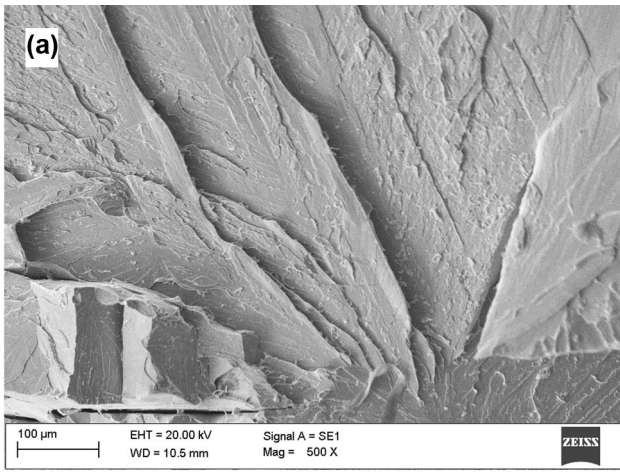


Fig. 8—Fracture surface of EF101 overlay weld. (a) illustrates mainly transgranular fracture paths (vertical, Z axis), while (b) shows also fractures in the transverse direction (horizontal, X axis) crossing the transgranular planes.

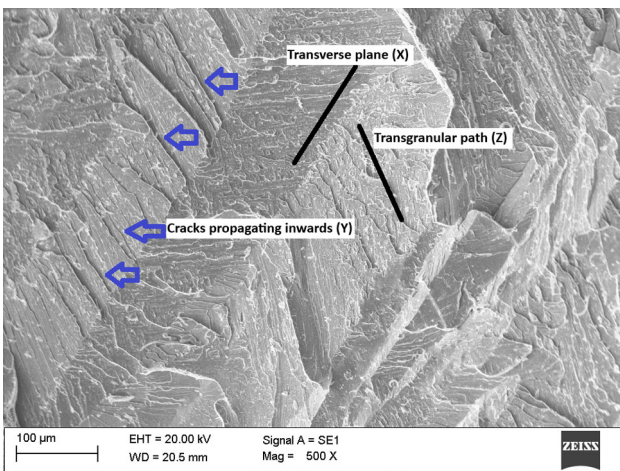


Fig. 9—Fracture surface in APMT overlay weld. Additional cracks propagating inwards, perpendicularly to the transgranular and to the transverse directions (blue arrows) (Color figure online).

Table VII shows the hardness results ( $HV_{0.3}$ ) for the lab furnace heat treated samples. The length of the heat treatment selected (11 days, 42 days) is much shorter

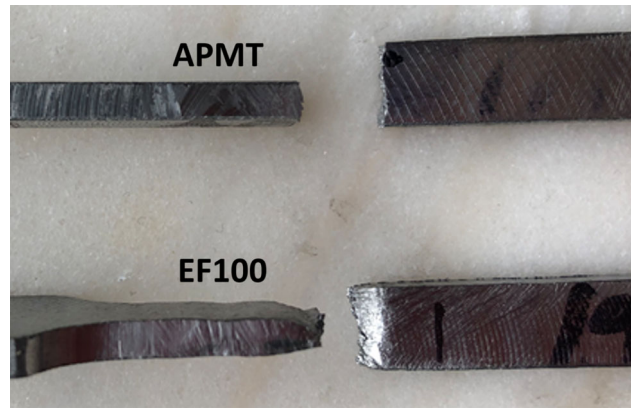
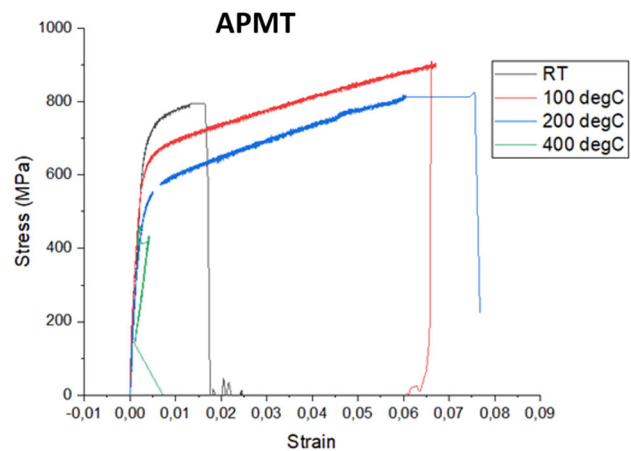
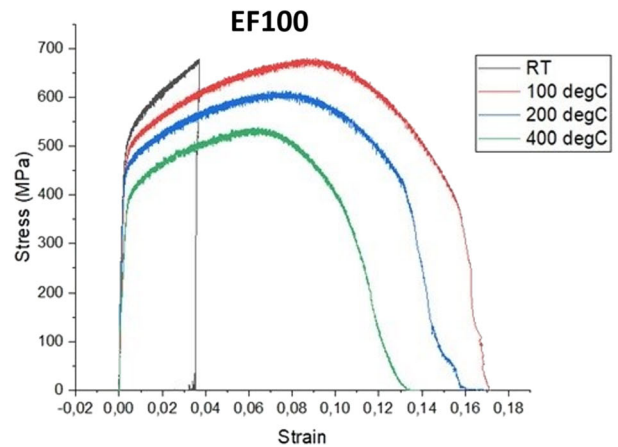


Fig. 10—Top and side view of the tensile tested coupons at room temperature. APMT showing a flat surface indicating very little or no plastic deformation, while the cup and cone fracture morphology in EF100 indicates some plastic deformation.



(a)



(b)

Fig. 11—Stress-strain diagrams at different temperatures. (a) corresponds to APMT and (b) corresponds to EF100.

than the boiler exposure (6 months), and the standard deviation is large, too. However, the mean values seem to confirm the trend of hardening for APMT and softening for EF100 after a few days at 400 °C.

**Table VI. Tensile Test Results (Single Values for APMT, Average Values for EF100)**

Material	Temperature (°C)	$\sigma$ 0.2 Pct (MPa)	UTS (MPa)	Elongation (Pct)
APMT	Room	751	790	1.8
	100	650	900	6.4
	200	548	819	7.7
	400	—	410	0
EF100	Room	563	678	3.1
	100	520	672	15
	200	490	605	13
	400	424	522	11

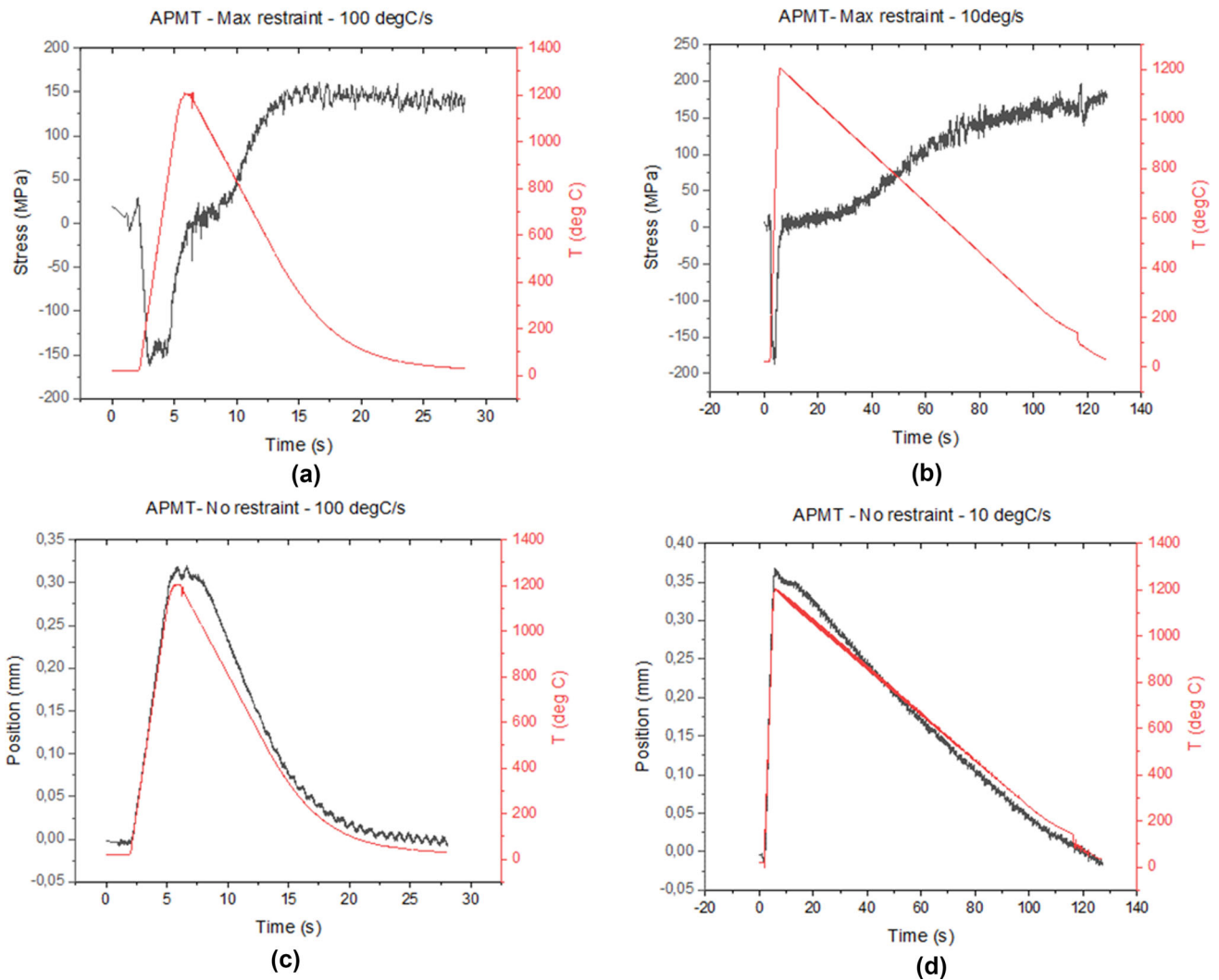


Fig. 12—APMT overlay weld response to the max. restraint test and to the no restraint test. (a) and (b) show the evolution of stress and temperature in the overlay in the max restraint test by applying 100 °C/s and 10 °C/s cooling rate, respectively. (c) and (d) show the deformation of the overlay and the temperature in the no restraint experiment by applying 100 °C/s and 10 °C/s cooling rate, respectively.

The APT investigation of the EF100 overlay revealed the presence of dislocations and the segregation of RE1 to dislocations (Figure 15). Segregation of RE1 happened for all the cases investigated: room temperature (as deposited), after 400 °C for 11 days, and after 400 °C for 42 days. Therefore, the segregation could not be associated with the heat treatment at 400 °C, but with

the overlay welding process. The atomic maps for Cr and for Si do not reveal a segregation of those atoms, as they appear homogeneously distributed in the samples analyzed.

For APMT overlay welds, MC carbides were found, being M: Mo, RE3, and RE7 in both conditions, as-deposited (room temperature) and at 400 °C for 11

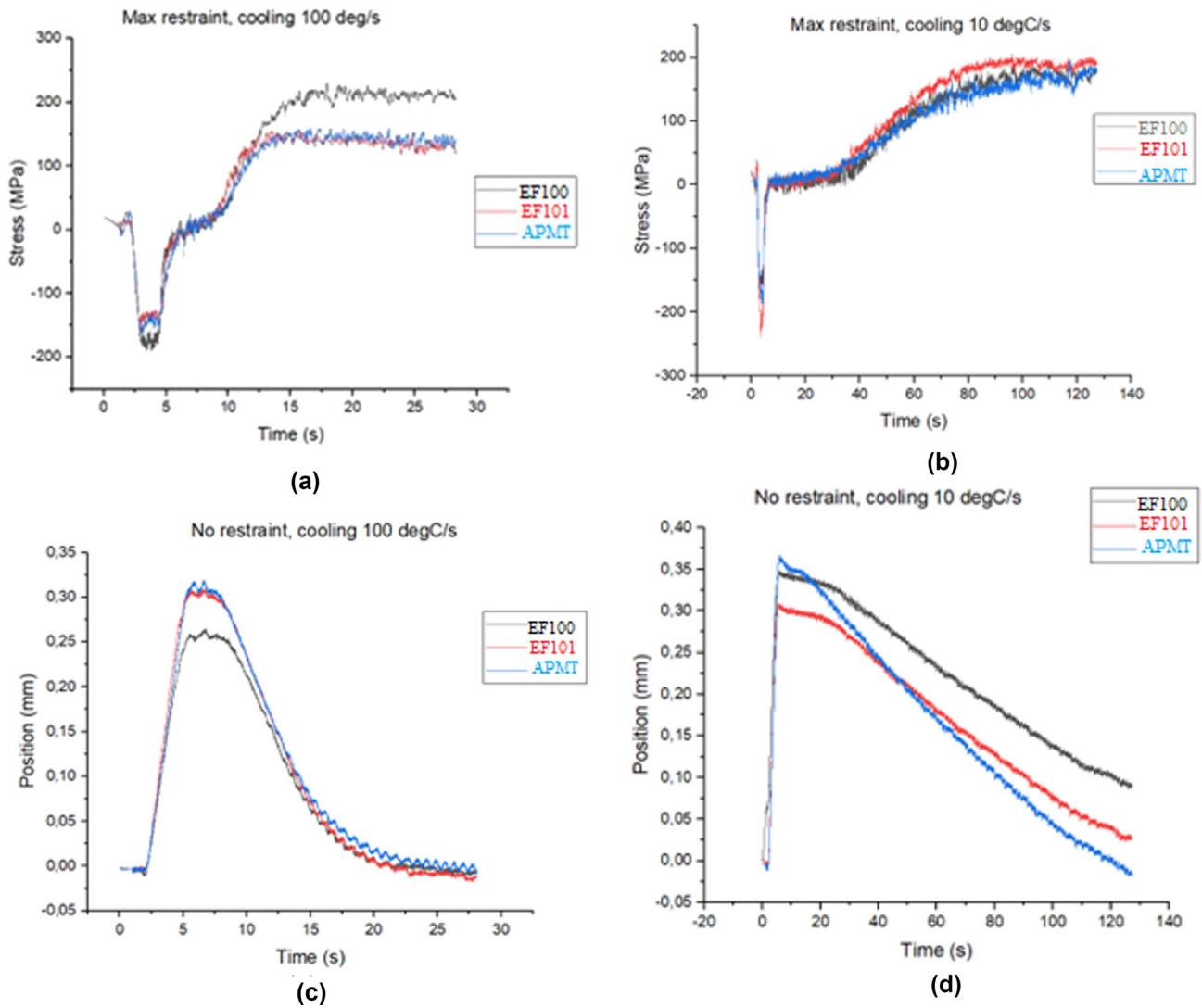


Fig. 13—Comparative response to the max. restraint test and to the no restraint test for the three FeCrAl alloys. (a) and (b) show the stress evolution during the max restraint test for the three FeCrAl alloys. (c) and (d) show the deformation of the FeCrAl alloys in no restraint condition. In (a) and (c) the cooling from the peak temperature (1200 °C) was performed at 100 °C/s. In (b) and (d), the cooling from the peak temperature (1200 °C) was performed at 10 °C/s. The faster speed of contraction was for APMT (blue), followed by EF101 (red) and the one with the slower slope was EF100 (black) (Color figure online).

days, meaning that the carbides were already formed during the solidification process that occurs in welding, and not by the heat treatment. Figure 16 shows the atomic maps revealing the C distribution and therefore, the presence of carbides before and after the heat treatment. Figure 17 presents the graphical representation of the atoms' concentration at certain distances from the carbides (proxigram) in overlaid APMT. The proxigram confirms the nature of the carbides as Mo, RE3, and RE7, and it shows that the Cr content around the carbide is very similar to the Cr content in the matrix, around 20 pct atomic for APMT overlay at room temperature [Figure 17(a)]. However, after being exposed at 400 °C for 11 days [Figure 17(b)], it is possible to observe that the Cr content increases up to 30 pct atomic in the area around the carbide after the exposure at 400 °C. This indicates that the carbides

could be initiation sites pushing toward the phase separation (Fe-rich  $\alpha$ -phase and Cr-rich  $\alpha'$ -phase).

Concerning the general microstructure of the FeCrAl overlay welds, the analysis of cross-sections confirmed the same morphology for their solidification structure, consisting of long columnar ferritic grains following the direction of heat dissipation (Figure 18).

The presence of cracks in the cross-sections of the overlay welds was investigated. In EF101 overlay welds, it was possible to find cracks propagating through the overlay and progressing to the substrate (Figure 19). The investigation of the cross-sections of the overlay welds of EF100 also showed some cold cracks (Figure 20). However, as a difference to alloy EF101, none of the cracks propagated through to the substrate. Cold cracks were also observed when inspecting cross-sections of APMT overlay welds, not only

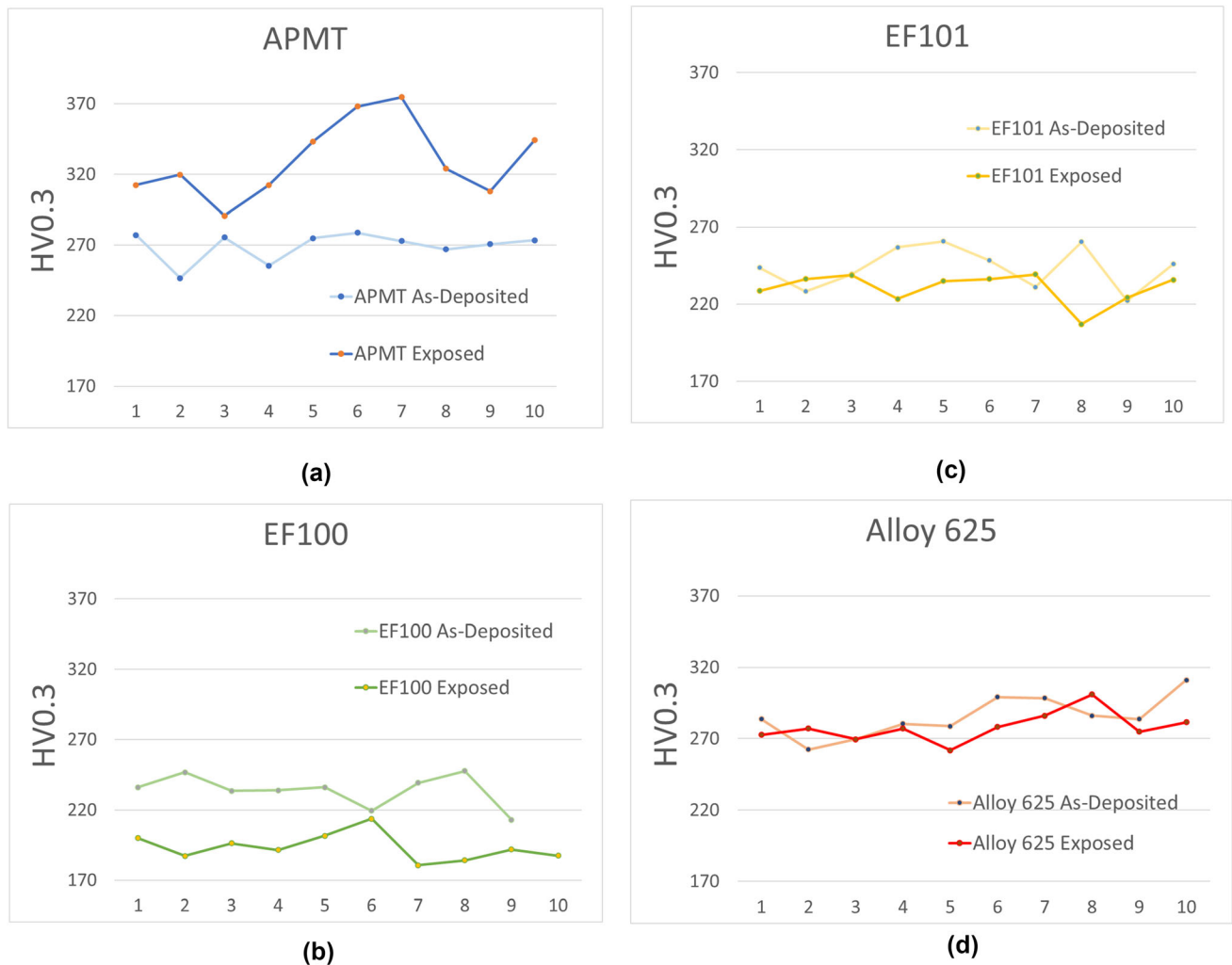


Fig. 14—Hardness ( $HV_{0.3}$ ) for each cladding alloy in the as-deposited (non-exposed) and in the exposed condition (as tube shield for 6 months). (a) corresponds to the hardness of APMT overlay, (b) to EF100 overlay, (c) to EF101 overlay, and (d) to alloy 625 overlay. The vertical scale range is kept constant (170 to 370  $HV_{0.3}$ ) for all the graphs to facilitate a visual comparison among the different alloys and conditions. The x-scale corresponds to testing positions as described in Figure 1.

**Table VII. Hardness Results (Mean Value and Standard Deviation) for the Furnace Heat Treated Samples**

Overlay Material	$HV_{0.3}$ Before Heat Treatment	Temperature ( $^{\circ}C$ )	Time (days)	$HV_{0.3}$ After Heat Treatment
APMT	$269 \pm 10$	400	11	$295 \pm 19$
EF100	$234 \pm 11$	400	11	$221 \pm 5$
			42	$216 \pm 8$

following the direction of the heat dissipation [Figure 21(a)], but also in parallel to the substrate (in the horizontal direction), as shown in Figure 21(b). From these results, it is clear that all the FeCrAl overlay welds are susceptible to cold cracking. However, the fact that cracks in the overlay do not propagate through the substrate or in parallel to the substrate seems to indicate that the susceptibility of alloy EF100 is lower than the rest of the alloys.

In terms of SEM-EDS microanalysis, the three types of FeCrAl overlays presented micro-nano precipitates in the grain boundaries, but also intragranularly. Those precipitates were rich in different RE.

When comparing the microstructure of EF101 overlays before and after the exposure in the boiler for 6 months, no differences were found. In both conditions, RE1, RE2, and RE3 were forming precipitates mainly in the grain boundaries, but also intragranularly (Figure 22).

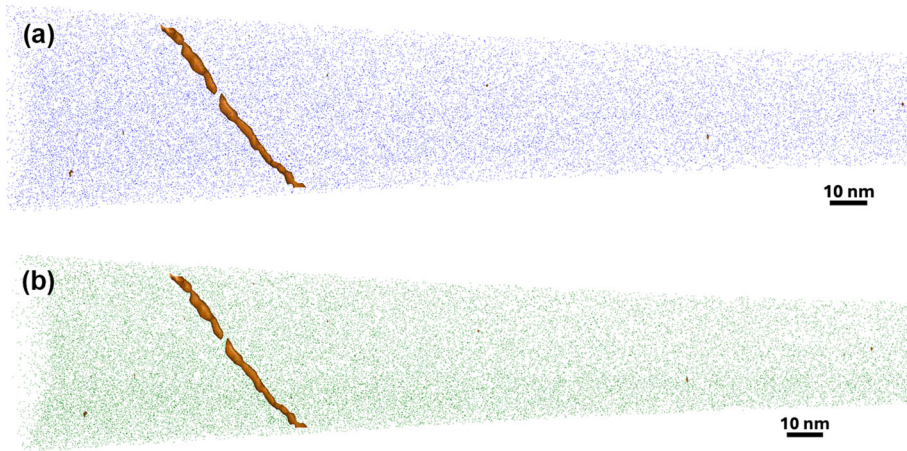


Fig. 15—Atomic maps of as-deposited EF100 overlay welded material, showing RE1 enrichment at a dislocation. The isosurface is 0.88 at. pct RE1 (brown color). (a) shows the Cr atomic map in blue, while (b) shows the Si atomic map in green.

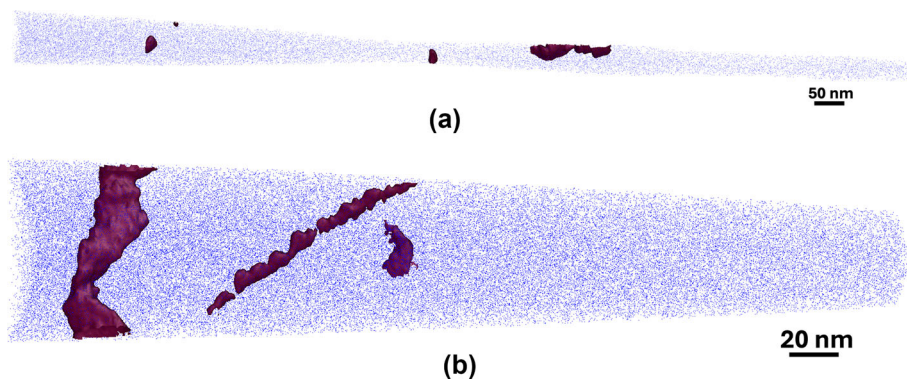


Fig. 16—Atomic maps in APMT overlay welded material. (a) corresponds to room temperature and (b) after 400 °C for 11 days. Cr atoms are shown in blue and carbon isosurfaces are shown in brown, with thresholds of 5.0 at. pct (a) and 2.6 at. pct (b).

The EF100 overlays before exposure showed a concentration of RA1, RA2, RA3, and RA4 precipitates in combination with Al and C, mainly located in the grain boundaries (Figure 23). After exposure in the boiler, RE1 and RE3 were found forming precipitates in the grain boundaries, but also intragranularly.

APMT overlays were the ones presenting more differences when comparing the microstructure before and after exposure in the boiler. Figure 24(a) shows the microstructure of APMT overlays before exposure in the furnace. Different types and sizes of precipitates were identified. In the range of 1  $\mu\text{m}$  size, precipitates containing RE2, RE5, RE6, and RE7 were identified. However, it was not possible to disclose the composition of the nano precipitates located in the grain boundaries and intragranularly [Figure 24(b)] with the available SEM-EDS equipment.

After exposure for 6 months in the boiler, precipitates with different morphologies were observed (Figure 25). The most noticeable difference with the unexposed material was the enrichment of Cr in the grain boundaries. Figure 26 shows the Cr enrichment in the grain boundary and the presence of RE2-Al as intragranular precipitate. An EDS line scan in the matrix crossing a

fusion boundary showed the presence of RE2, RE5, and RE6 in the grain boundary.

## IV. DISCUSSION

### A. The Relevance of Welding in the Mechanical Properties of the FeCrAl Alloys

By comparing the tensile properties at room temperature of commercially available APMT in its delivery condition (yield strength 540 MPa, tensile strength 740 MPa and elongation 26 pct)<sup>[6]</sup> with the tensile properties of the overlay welded APMT in this study [Table VI, Figure 11(a)], showing an elongation of 1.8 pct and a yield strength 751 MPa, it is clear that welding strongly influences on the resulting ductility. Although alloys EF100 and EF101 are recently developed and lack comparable data, it is likely that welding these alloys also leads to a drastic reduction in ductility due to the fast solidification and cooling inherent to welding.

The restraint-cooling experiment in the thermo-mechanical simulator was an attempt to register the response of undiluted overlay welded FeCrAl alloys to the restraint and cooling conditions caused by the

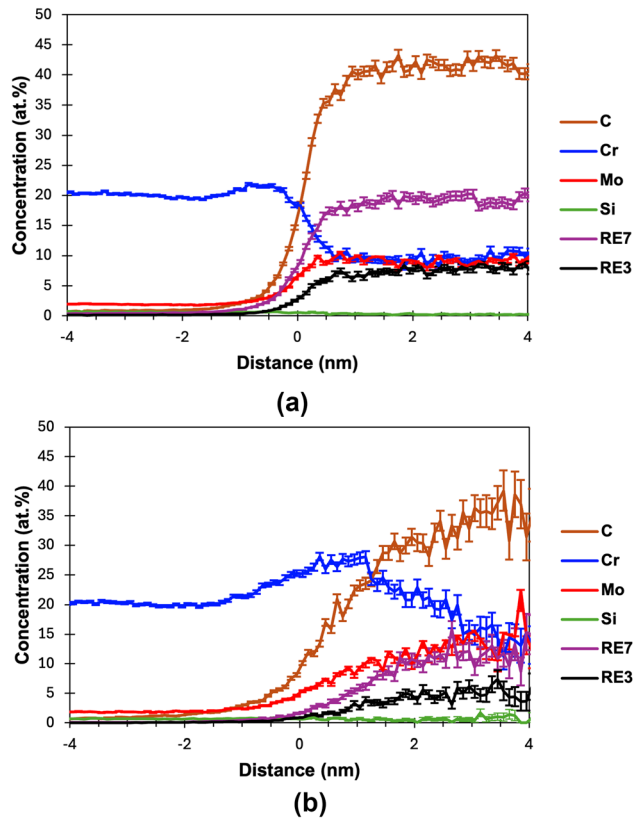


Fig. 17—Proxigrams around the carbides in APMT. (a) shows that the Cr content close to the carbide is similar to the matrix (20 pct atomic) at room temperature, while (b) indicates that the Cr content increases up to 30 pct atomic after the material was exposed after 400 °C for 11 days.

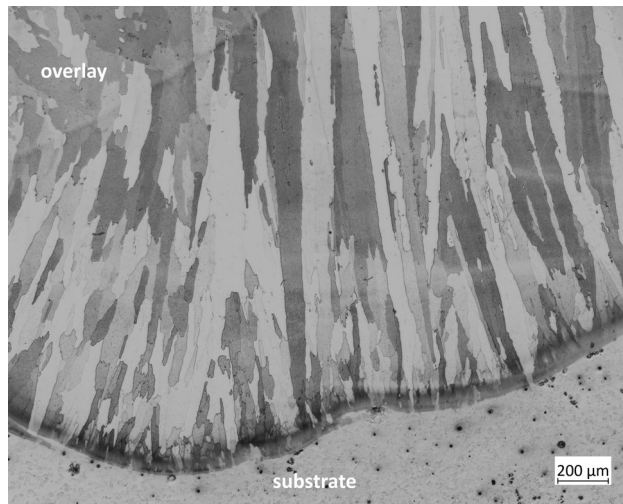


Fig. 18—Cross-section of EF101 FeCrAl overlay (etched), SEM image showing long columnar grains.

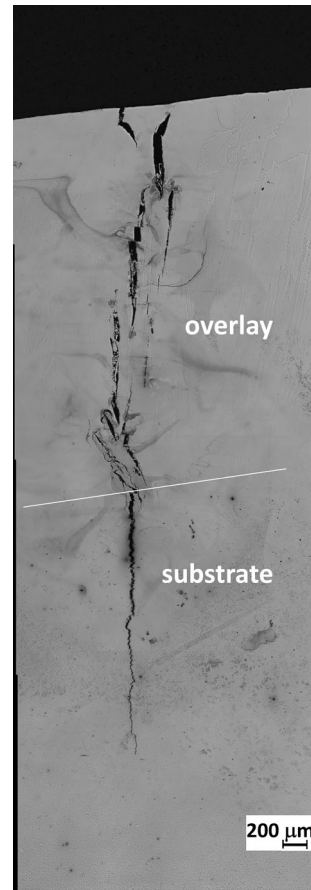


Fig. 19—LOM cross-section of overlay weld EF101 (unetched).

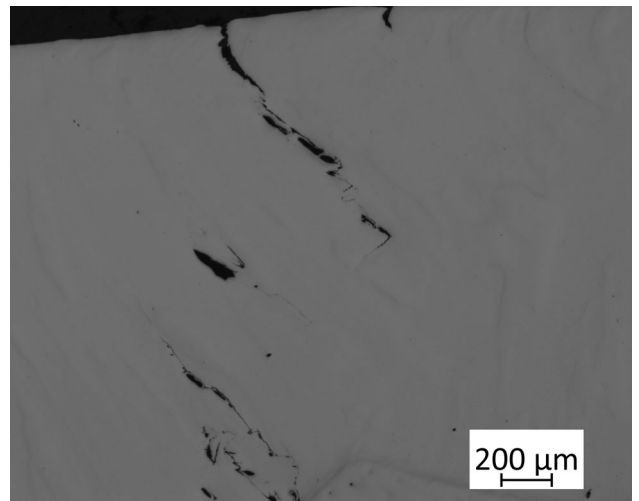
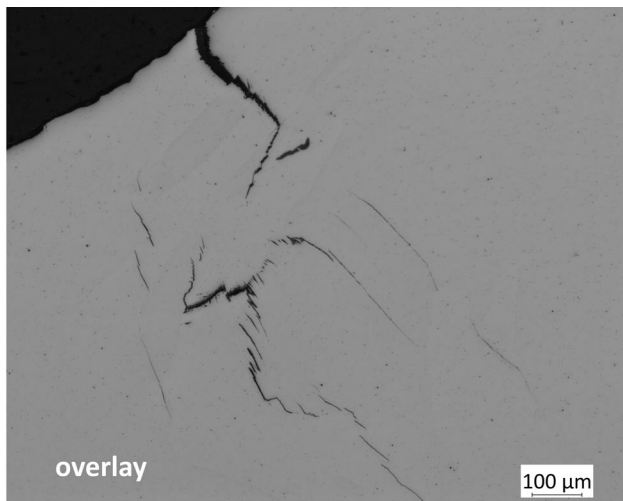
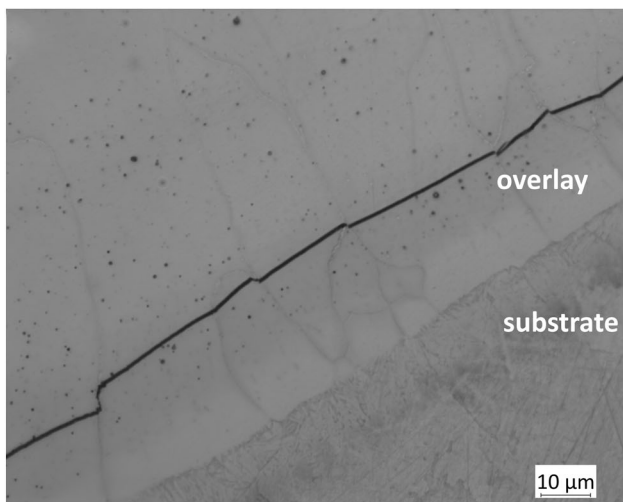


Fig. 20—LOM cross-sections of the overlay weld EF100 (unetched) showing cold cracking phenomenon in the clad but not propagating to the substrate.



(a)



(b)

Fig. 21—LOM cross-sections of APMT overlay weld (unetched) showing cold cracking phenomenon. (a): cracks mainly following the solidification direction in the overlay. (b): Right: long crack along the overlay in parallel to the substrate.

welding process. The maximum restraint experiment tried to reproduce the restraints occurring during welding, when the deposited material can not expand due to the substrate underneath and the previously deposited weld beads on the sides. In those conditions, the cooling rate made a difference in the stress that the alloys could withstand. At a slow cooling rate (10 °C/s), the three FeCrAl alloys showed a very similar level of residual stresses [Figure 13(b)], but at a faster cooling rate (100 °C/s), which is more aligned with arc-welding, EF100 could cope with higher stresses than the rest of

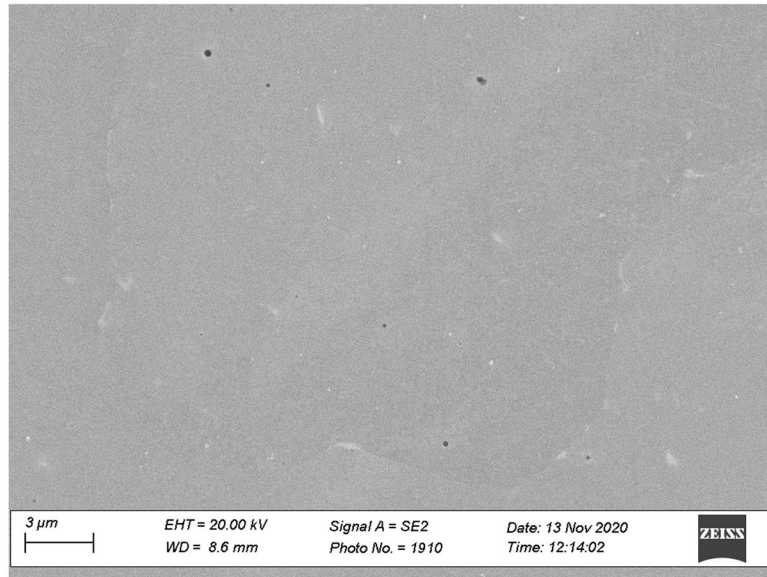
alloys [Figure 13(a)]. The cooling rate experienced by the welds is related to the arc energy used, which is a direct consequence of the welding settings (voltage, amperage, travel speed).<sup>[29]</sup> The different response of the FeCrAl alloys to the cooling rates during solidification opens the door to research in the optimization of the welding process to minimize the occurrence of cracks.

### B. Ductility of the Overlay Welds

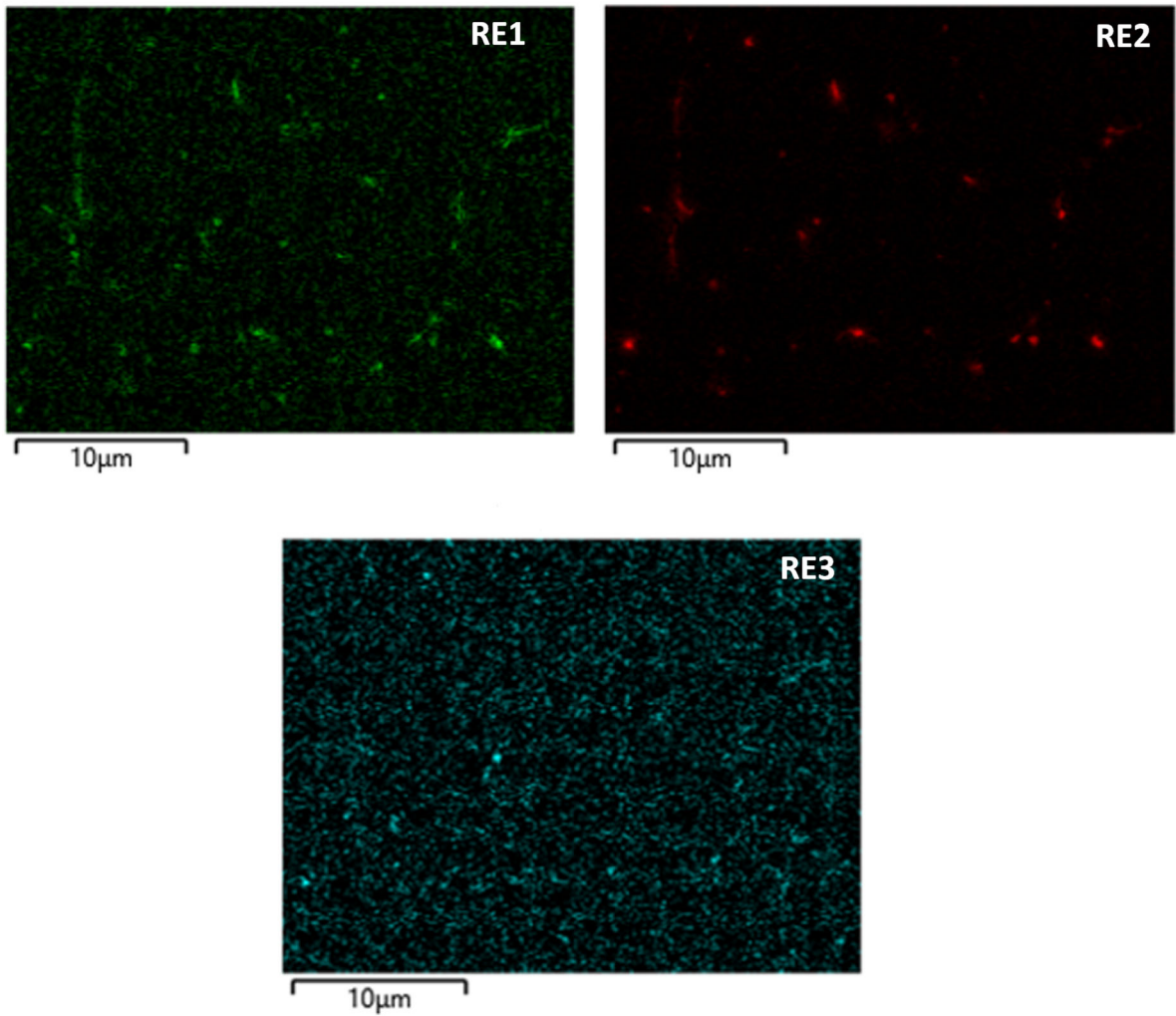
The results presented in the “[Ductility of the Overlay Welds: Bend Test, Fractography and High Temperature Tensile Test](#)” section, *i.e.*, the bending angle to fracture, the analysis of the fracture surfaces, and the tensile test results, are in full alignment, and they support the grading of the FeCrAl overlay welds from higher to lower ductility as follows: EF100 > EF101 > APMT. The results from the restraint-cooling test (see the “[Influence of Cooling Rate and Restraint Conditions on the Ductility of FeCrAl Undiluted Overlays](#)” section) also support this grading, as EF100 was the alloy showing less deformation under no-restraint conditions and under maximum restraint and faster cooling. EF100 was the alloy that withstood higher stresses, as already mentioned. In any case, the results from the tensile test (Table VI, Figure 11) suggest that these FeCrAl alloys have a high ductile-to-brittle transition temperature, somewhere between room temperature and 100 °C, which is an indication of the low ductility and therefore high cold cracking susceptibility. The occurrence of cold cracks observed in the cross-sections of the overlay welds (Figures 19, 20, and 21) and the fractographic analysis (Figures 7, 8, and 9) was again in alignment with the previous grading of the alloys. In APMT overlay welds, cracks were found following the solidification direction, but also in parallel to the substrate. In EF101, some cracks propagated through the entire overlay and the substrate.

It is known from the literature that Cr and Al contents play a role in the cracking susceptibility of FeCrAl overlay clads.<sup>[20]</sup> The more Cr and Al in the alloy, the higher the susceptibility to cold cracking. The FeCrAl alloys investigated had very similar Al content (4 pct) all of them, but there was a difference in the Cr content between APMT (21 pct), EF101 (12.5 pct) and EF100 (10 pct), which can be related to their cracking susceptibility as proposed in the literature.<sup>[19,20]</sup>

According to literature,<sup>[30]</sup> in general, Si can form several silicides (FeSi, Fe<sub>2</sub>Si, Fe<sub>3</sub>Si, Fe<sub>5</sub>Si) and a Cr<sub>3</sub>Si intermetallic. All of them tend to embrittle during solidification, forming low-melting eutectic constituents, particularly with Ni. For this reason, despite being added to improve oxide scaling resistance at elevated

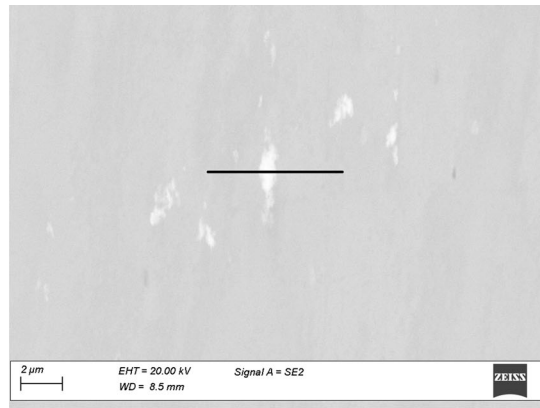


(a)

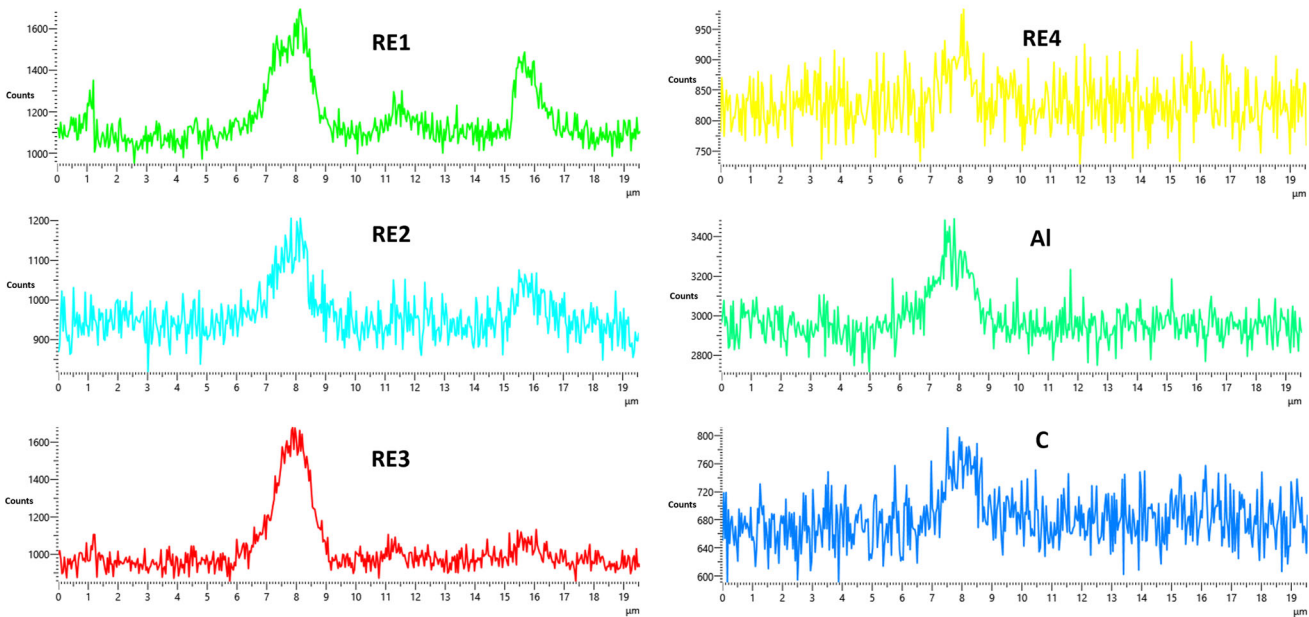


(b)

Fig. 22—Microstructure of EF101 overlay. (a) is the SEM image (unetched) before exposure, and (b) is the EDS elementary mapping of the whole area in (a), showing the presence of REs mainly concentrating in the grain boundaries (bright in the image).



(a)



(b)

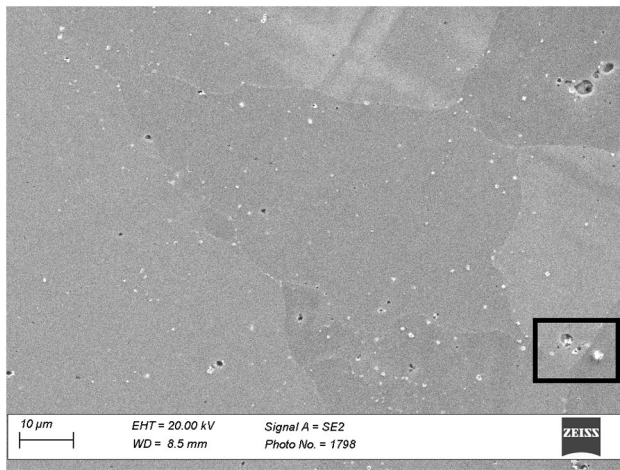
Fig. 23—Microstructure of EF100 overlay. (a): SEM (unetched) showing precipitates in the grain boundaries before exposure. (b): EDS line scan crossing the grain boundary as indicated by the black line in (a). It shows the presence of four species of RE as well as C and Al in the precipitates.

temperatures, it is normally held below 1 pct.<sup>[30]</sup> This reasoning could support the lower ductility of EF101 with higher Si content, compared to EF100 with lower Si content. However, in this work, it was not possible to identify those intermetallics with SEM-EDS, and APT in EF100 showed a homogeneous atom map for Si. It is also expected that Al and Si contribute to the solid solution strengthening of these alloys.<sup>[31]</sup> Both EF100 and EF101 have similar Al content, and what has been found is the combination of Al with several REs in EF100 (Figure 23), and the combination of Al-RE6 (Figure 26) and Si with several REs (Figure 27) in the

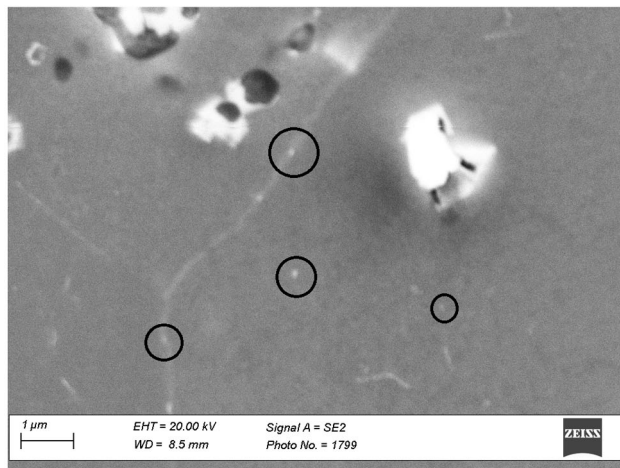
case of APMT. The complex microstructure resulting from the fast cooling and the presence of REs both in the grain boundaries, but also intra granularly, would require additional investigation to correlate the microstructure with the differences in ductility observed.

### C. Influence of the Boiler Exposure on the Hardness

The hardness of the non-exposed and exposed EF100, EF101, APMT, and Alloy 625 overlay welds confirm that EF101 and Alloy 625 hardness are not affected significantly by the temperature and exposure conditions



(a)



(b)

Fig. 24—SEM images (unetched) of APMT overlay before exposure in the furnace. (a) gives an idea of the diversity of size and distribution of the precipitates, and (b) is a higher magnification of the square area in (a), showing nano precipitates (black circles) that were not possible to be analyzed.

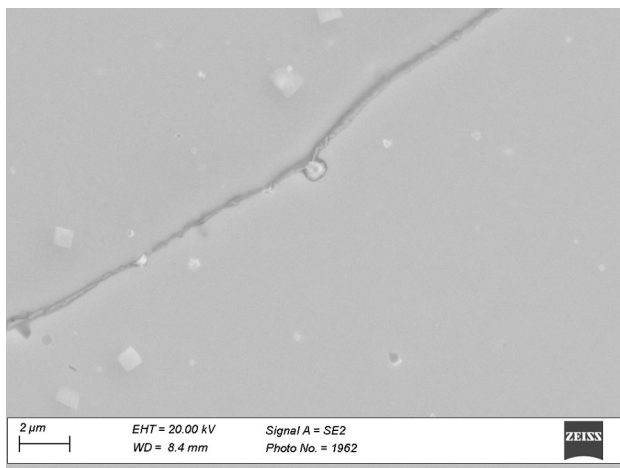


Fig. 25—SEM image (unetched) of the exposed overlay APMT, showing REs precipitates both in the grain boundary and intra granularly.

in the boiler, while alloy EF100 experiences softening and APMT experiences hardening during the 6-month exposure in the boiler (Figure 14). Hardness performed on samples that were exposed for shorter times (11 days and 42 days) also indicated a trend in hardening for APMT and softening for EF100 overlay welds (Table VII).

The evolution of hardness in EF100, EF101, and APMT during exposure is believed to be mainly the result of two competing processes: softening through recovery, and hardening through phase separation of the ferritic matrix, the latter being the cause of 475 °C embrittlement.

At temperatures below 500 °C, the matrix of ferritic steels with high Cr will decompose into an Fe-rich  $\alpha$ -phase and a Cr-rich  $\alpha'$ -phase. This causes significant hardening and leads to “475 °C embrittlement.”<sup>[32–34]</sup> The phenomenon is well-known in conventional FeCrAl alloys containing around 20 pct Cr, such as APMT.

In APMT overlays is where the microstructure experiences more variation when comparing the as-deposited and the exposed conditions, especially the concentration of Cr in the grain boundaries (Figure 26). The APT results for APMT were not conclusive in showing the phase separation after being exposed at 400 °C for 11 days, but Cr enrichment in the areas around the carbides was observed, and that could be the first sign of the initiation of phase separation. All these could explain the hardening of the alloy during exposure in the boiler.

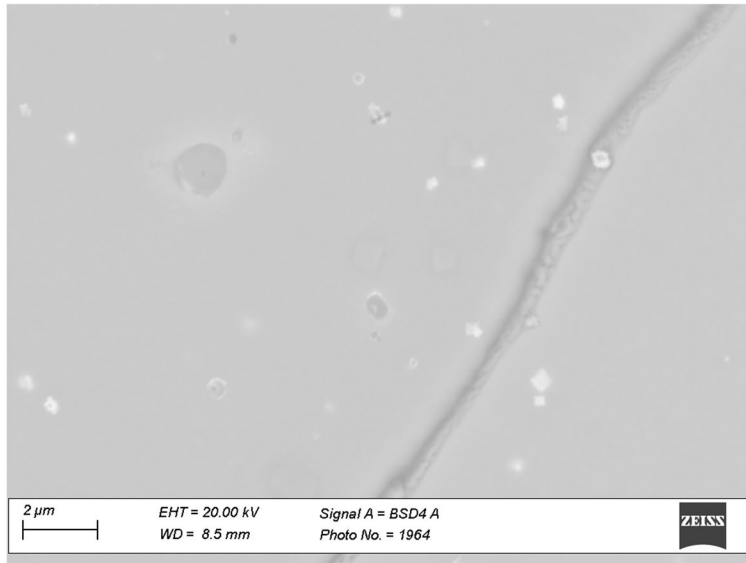
EF100 and EF101 were designed with lower Cr to avoid this embrittlement. EF100 and EF101 seem to present differences in the morphology of the RE precipitates after exposure, likely triggered by the prolonged time at temperature,<sup>[35]</sup> but additional investigation with EPMA would be required for a deeper analysis.

APMT and Alloy 625 showed higher hardness values compared to EF100 and EF101, and interestingly, those were the alloys that presented better performance against the erosive-corrosive environment in the boiler, as presented in another of the authors’ paper.<sup>[36]</sup>

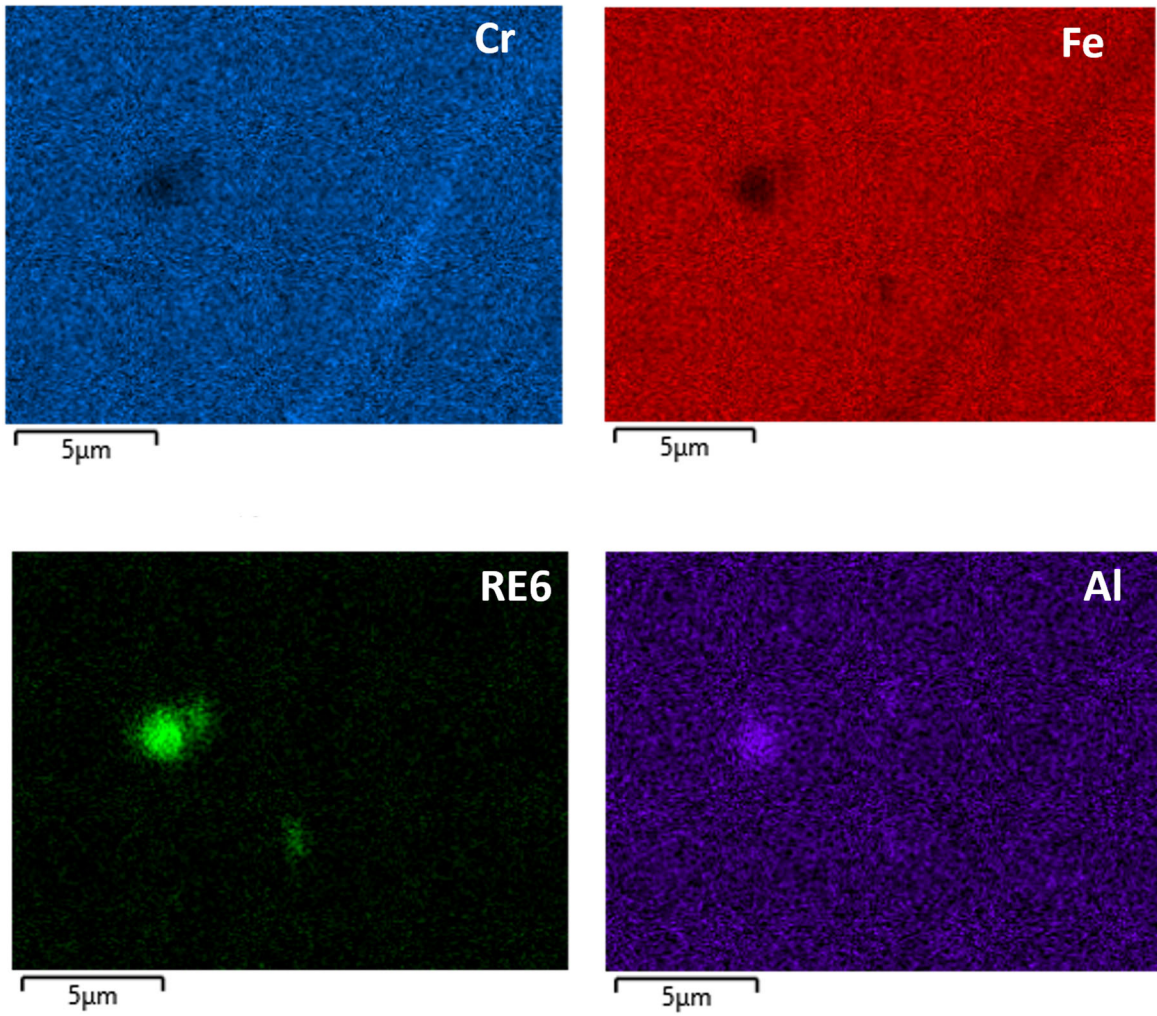
## V. CONCLUSION

Three FeCrAl alloys (EF100, EF101, and APMT) were used to prepare overlay welds to be exposed for 6 months in the evaporator tube bank of a CFB boiler. This work focused on the performance of these alloys in the as-deposited condition and after being exposed to high temperature conditions in the boiler. The main conclusions are summarized:

1. Based on the results of the bending angle to fracture, the fracture morphology, and the tensile tests, the ductility of the overlay welds could be graded from higher to lower ductility as follows: EF100 > EF101 > APMT.
2. The high temperature tensile tests concluded that the three alloys have a high ductile-to-brittle transition temperature, somewhere between room



(a)



(b)

Fig. 26—Microstructure of exposed overlay APMT. (a): SEM (unetched) and (b): EDS elementary mapping of the whole area in (a), showing the Cr enrichment and Fe depletion in the grain boundary, and also the presence of RE6-Al precipitates intra granularly.

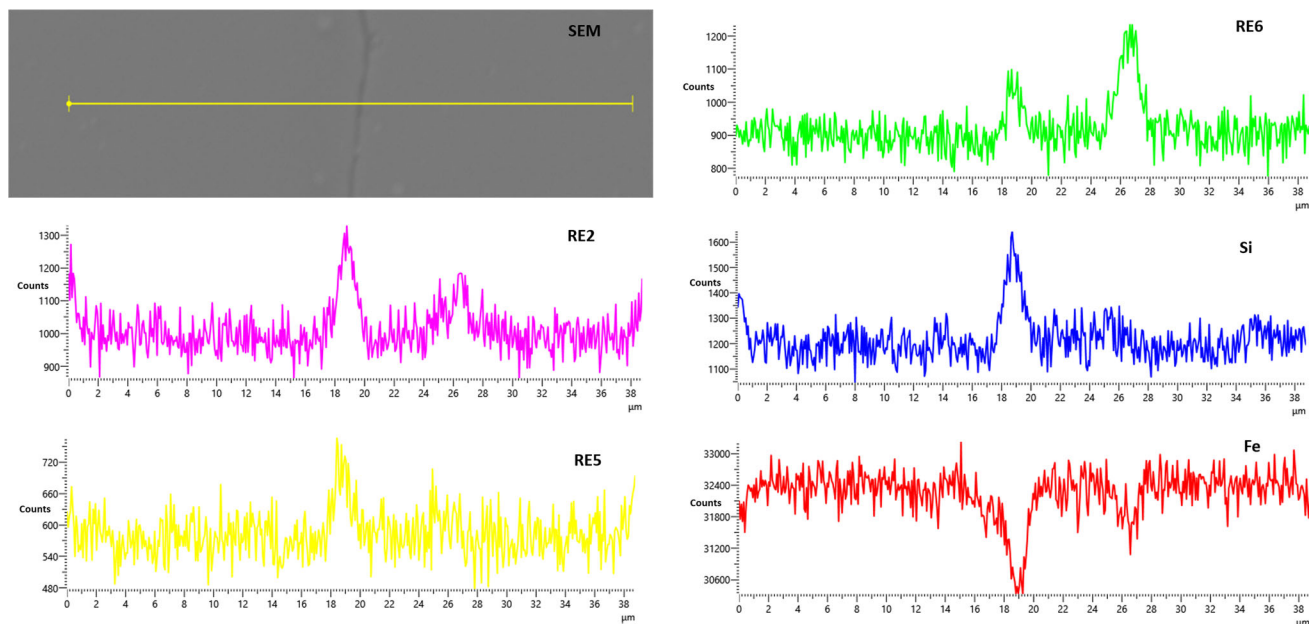


Fig. 27—SEM-EDS line scan of exposed overlay APMT, revealing the presence of RE2, RE5, and RE6 in the grain boundary.

temperature and 100 °C, and the restraint-cooling test showed that under high restraint conditions and fast cooling rates, simulating welding conditions, EF100 overlays can withstand higher stresses than the rest of the FeCrAl alloys.

- EF101 and Alloy 625 hardness are not clearly affected by the temperature and exposure conditions in the boiler, while alloy EF100 experiences softening and APMT experiences hardening. Atom Probe Tomography showed that the exposure of APMT at 400 °C for 11 days resulted in higher Cr concentration around carbides than in the matrix. That can indicate that carbides could be initiation sites pushing toward the phase separation (Fe-rich  $\alpha$ -phase and Cr-rich  $\alpha'$ -phase), resulting in a drastic reduction in APMT ductility.

#### ACKNOWLEDGMENTS

Alleima AB (formerly Sandvik Materials Technology AB), Navium Energi AB (formerly E.ON Värme Sverige AB) and Kanthal AB are gratefully acknowledged for their participation in this research project by providing the filler materials, facilitating the on-site exposures of the overlay welds in the waste-fired power plant, and for the valuable discussions. Therefore, warm acknowledgement to Anna Jonasson (Navium Energi), Mette Frodigh (Alleima), and Rickard Shen (Kanthal). Research Engineer Kjell Hurtig is gratefully acknowledged for the preparation of the overlay welds and for his support with the heat treatment furnaces at University West. PhD researcher Gökce Aydin is also gratefully acknowledged for her

support in sample preparation for the APT samples. The APT analyses were conducted at Chalmers Materials Analysis Laboratory (CMAL).

#### FUNDING

Open access funding provided by University West. This work was funded by the Stiftelsen för Kunskaps och Kompetensutveckling (KK-stiftelsen) under Grant reference 20170316, named HÖG-FECRALCLAD Svetsbarhet och korrosionbeständighet av nya FeCrAl-legeringar.

#### CONFLICT OF INTEREST

The authors declare that they have no conflict of interest.

#### OPEN ACCESS

This article is licensed under a Creative Commons Attribution 4.0 International License, which permits use, sharing, adaptation, distribution and reproduction in any medium or format, as long as you give appropriate credit to the original author(s) and the source, provide a link to the Creative Commons licence, and indicate if changes were made. The images or other third party material in this article are included in the article's Creative Commons licence, unless indicated otherwise in a credit line to the material. If material is not included in the article's Creative Commons licence and your intended use is not permitted by statutory regulation or exceeds the permitted use, you will need to obtain permission directly from the copyright

holder. To view a copy of this licence, visit <http://creativecommons.org/licenses/by/4.0/>.

## REFERENCES

1. F. Cherubini, S. Bargigli, and S. Ulgiati: *Energy*, 2009, vol. 34, pp. 2116–23.
2. L. Levaggi, R. Levaggi, C. Marchiori, and C. Trecroci: *Sustainability*, 2020, vol. 12, p. 5743.
3. R.H.J.M. Gradus, P.H.L. Nillesen, E. Dijkgraaf, and R.J. van Koppen: *Ecol. Econ.*, 2017, vol. 135, pp. 22–28.
4. COMMUNICATION FROM THE COMMISSION TO THE EUROPEAN PARLIAMENT, THE COUNCIL, THE EUROPEAN ECONOMIC AND SOCIAL COMMITTEE AND THE COMMITTEE OF THE REGIONS Managing Climate Risks - Protecting People and Prosperity, 2024.
5. Kanthal® APM Wire — Kanthal®, <https://www.kanthal.com/en/products/material-datasheets/wire/resistance-heating-wire-and-resistance-wire/kanthal-apm/>, (accessed 17 December 2024).
6. Kanthal® APMT Tubes — Kanthal®, <https://www.kanthal.com/en/products/material-datasheets/tube/kanthal-apmt/>, (accessed 17 December 2024).
7. H. Worch: *Cryst. Res. Technol.*, 1989, vol. 24, p. 378.
8. B. Jönsson and A. Westerlund: *Oxid. Met.*, 2017, vol. 88, pp. 315–26.
9. F.H. Stott, G.C. Wood, and J. Stringer: *Oxid. Met.*, 1995, vol. 44, pp. 113–45.
10. K.G. Field, X. Hu, K.C. Littrell, Y. Yamamoto, and L.L. Snead: *J. Nucl. Mater.*, 2015, vol. 465, pp. 746–55.
11. K.G. Field, S.A. Briggs, K. Sridharan, R.H. Howard, and Y. Yamamoto: *J. Nucl. Mater.*, 2017, vol. 489, pp. 118–28.
12. K.G. Field, K.C. Littrell, and S.A. Briggs: *Scr. Mater.*, 2018, vol. 142, pp. 41–45.
13. M.N. Gussev, E. Cakmak, and K.G. Field: *J. Nucl. Mater.*, 2018, vol. 504, pp. 221–33.
14. X. Wu, T. Kozlowski, and J.D. Hales: *Ann. Nucl. Energy*, 2015, vol. 85, pp. 763–75.
15. Y. Yamamoto, B.A. Pint, K.A. Terrani, K.G. Field, Y. Yang, and L.L. Snead: *J. Nucl. Mater.*, 2015, vol. 467, pp. 703–16.
16. H. Kinnunen, M. Hedman, D. Lindberg, S. Enestam, and P. Yrjas: *Energy Fuels*, 2019, vol. 33, pp. 5859–66.
17. Y. Alipour and P. Henderson: *Corros. Eng. Sci. Technol.*, 2015, vol. 50, pp. 355–63.
18. Y. Alipour, A. Talus, P. Henderson, and R. Norling: *Fuel Process. Technol.*, 2015, vol. 138, pp. 805–13.
19. J.R. Dupont, J.R. Regina, and K. Adams, eds.: in *21st Annual Conference on Fossil Energy Materials*, Knoxville, Tennessee, 2007, pp. 132–37.
20. J.R. Regina, J.N. Dupont, and A.R. Marder: *Weld. J.*, 2007, vol. 86, pp. 170s–78s.
21. W. Li, S. Lu, Q.-M. Hu, H. Mao, B. Johansson, and L. Vitos: *Comput. Mater. Sci.*, 2013, vol. 74, pp. 101–06.
22. S. Kobayashi and T. Takasugi: *Scr. Mater.*, 2010, vol. 63, pp. 1104–07.
23. C. Capdevila, M.K. Miller, G. Pimentel, and J. Chao: *Scr. Mater.*, 2012, vol. 66, pp. 254–57.
24. C. Capdevila, M.K. Miller, K.F. Russell, J. Chao, and J.L. González-Carrasco: *Mater. Sci. Eng. A*, 2008, vol. 490, pp. 277–88.
25. J. Ejenstam, M. Thuvander, P. Olsson, F. Rave, and P. Szkalos: *J. Nucl. Mater.*, 2015, vol. 457, pp. 291–97.
26. M.F. Gittos, V. Kumar, and Q. Lu: Effect of iron content on metallurgical and corrosion properties of Ni-Cr-Mo alloy weld overlays, IIW Document II-2043-2017 Annual Assembly of the International Institute of Welding, Shanghai, July 2017.
27. C.C. Silva, H.C. de Miranda, M.F. Motta, J.P. Farias, C.R.M. Afonso, and A.J. Ramirez: *J. Mater. Res. Technol.*, 2013, vol. 2, pp. 228–37.
28. J. Chao and C. Capdevila: *Metals*, 2020, vol. 10, p. 87.
29. C.L. Jenney and A. O'Brien: *Welding Handbook*, vol. 1, 9th edn.
30. J. Lippold and D. Kotecki: *Welding Metallurgy and Weldability of Stainless Steels*, Wiley, Hoboken, 2005.
31. Q. Lu, W. Xu, and S. van der Zwaag: *Comput. Mater. Sci.*, 2014, vol. 84, pp. 198–205.
32. T.G. Gooch, J.C.M. Farrar, and A.W. Marshall: *Weld. World*, 1995, vol. 35, pp. 248–54.
33. M.O. Malone: *Weld. J.*, 1967, pp. 241s–53s.
34. T.J. Nichol, A. Datta, and G. Aggen: *Metall. Trans. A*, 1980, vol. 11, pp. 573–85.
35. Norling, Rikard, Hjörnhede, Anders, and Mattsson, Mattias: *Long Term Testing of Materials for Tube Shielding, Stage 2.*, Värmeforsk Service AB, 2012.
36. M.A. Valiente Bermejo, A.M. Núñez, and R. Norling: *Mater. Corros.*, 2024, vol. 75, pp. 950–64.

**Publisher's Note** Springer Nature remains neutral with regard to jurisdictional claims in published maps and institutional affiliations.